Nature Communications

https://doi.org/10.1038/s41467-026-68947-7

Article in Press

RiboBright reveals cell-type-specific differences in ribosome organization and movement

Received: 30 April 2025

Accepted: 15 January 2026

Cite this article as: Poulladofonou, G., Grandi, C., Hu, X. *et al.* RiboBright reveals cell-type-specific differences in ribosome organization and movement. *Nat Commun* (2026). https://doi.org/10.1038/s41467-026-68947-7

Georgia Poulladofonou, Carmen Grandi, Xinyu Hu, Phillip Yesley, Willem A. Velema & Maike M. K. Hansen

RiboBright reveals cell-type specific differences in ribosome organization and movement

Georgia Poulladofonou,[1]# Carmen Grandi,[1,2]#, Xinyu Hu,[1,2]# Phillip Yesley,[1] Willem A. Velema,[1]* and Maike M. K. Hansen[1,2]*

[1] Institute for Molecules and Materials, Radboud University, Heyendaalseweg 135, 6525 AJ Nijmegen, the Netherlands.
[2] Oncode Institute, Nijmegen, The Netherlands
#These authors contributed equally
* willem.velema@ru.nl; maike.hansen@ru.nl

ABSTRACT

Ribosomes are responsible for protein synthesis in all living systems. Determining their cellular organization, movement and translational activity is crucial for dissecting ribosomes' complex functions. In this study, we describe the development of a selective fluorescent probe for eukaryotic ribosomes — RiboBright. Using C-H activation, the natural product cycloheximide was aminated at the C13-position and fluorescently modified to afford RiboBright. We employ RiboBright for quantification of ribosome content in 10 cell lines through microscopy and flow cytometry. RiboBright is applicable in live cells for tracking and quantification of ribosome movement and in fixed cells for visualization of sub-micrometer sized spots, at the single cell level. Strikingly, RiboBright reveals lineage-specific ribosome content, organization, and movement upon differentiation into either extraembryonic endoderm or ectoderm-like lineages. Thus, RiboBright provides a versatile and convenient approach for imaging the cellular dynamics of ribosomes.

KEYWORDS

Translation, Ribosome, Fluorescent probe, Differentiation, Cell-fate, Single-molecule, Live-cell Ribosomal tracking

INTRODUCTION

Ribosomes are the most abundant cellular component and essential macromolecular machines responsible for translating genetic information into proteins.[1] Historically ribosomes have been considered uniform entities that—though tightly regulated—themselves exhibit little capacity for regulation. However, recent technological advancements have uncovered surprising variability in ribosomal functioning between individual cells.[2-4] This variability, appears connected to variations in rRNA modifications and ribosomal protein composition, among other things.[5, 6] Furthermore, ribosome levels as well as localization vary significantly across different cell types and physiological states, necessitating tight regulation of ribosome biogenesis.[7-9] These differences, in turn, can influence the translation of specific mRNA subsets, suggesting that ribosomes play more specialized roles in cellular function than previously thought.[10, 11] This expanding view of ribosomal variability has spurred interest in studying how ribosome concentration and composition affect translation dynamics and cell-to-cell variability. For instance, in stem cells, transcription of ribosomal DNA (rDNA) is thought to be finely tuned to influence cell identity and fate.[12] Conversely, cancer cells can exhibit alterations in ribosome biogenesis to confer specific advantages such as rapid cell growth.[13-16]

Despite their functional importance, studying ribosomes in live cells has been challenging. Most current techniques, such as ribosome profiling and SILAC,[17-19] provide valuable insights into translation, but lack the spatial and temporal resolution to capture ribosomal dynamics at the single-cell level. Few fluorescent dyes that intercalate with RNA based on quinolinium[20] and naphtalimide[21] scaffolds have been developed, yet act unselectively. Moreover, most single-cell studies are limited to fixed cells by adapting fluorescent *in situ* hybridization[22] or focus on imaging newly synthesized proteins[23, 24], rather than directly visualizing ribosomes in live cells. While immunofluorescence studies do exist, they too are in fixed cells with the additional challenge of producing ribosome-specific antibodies.[25, 26] These studies often investigate changes in ribosome levels by targeting individual ribosomal proteins (RPs), as oppose to quantifying entire ribosomal subunits. Since these components are not always produced at equivalent rates,[27] measuring the concentration of non-rRNA elements may not accurately reflect the levels of ribosomes. Recent elegant advancements in live cell ribosome tracking have begun to address some of these challenges, yet these techniques are often difficult to set up and can be limited to a small number of targets.[28-32]

Here, we present the development and validation of a small molecule, RiboBright, which upon selectively binding to the 60S subunit of ribosomes increases in fluorescence in both live and fixed cells. RiboBright offers several key advantages, including rapid and reversible binding, making it highly versatile for a wide range of applications in studying ribosomal dynamics at a single-cell level. By combining live-cell imaging and tracking of ribosomal foci, we identify distinct diffusive behaviors, providing insights into ribosome movement within cells. With RiboBright, we quantify ribosome content and explore ribosome dynamics in a total of 10 different cell types (both human and mouse). We find that protein synthesis does not necessarily correlate with ribosome concentration within each cell line and across all 10 cell types, showing that high ribosome concentration is not predictive of high protein synthesis. Interestingly, embryonic stem cells show the lowest translational activity of ribosomes which increases upon differentiation. Furthermore, RiboBright reveals lineage-specific differences in ribosome diffusion, localization, and abundance

that emerge during stem cell differentiation. Together, these data demonstrate the versatility of RiboBright and reveal that ribosome content, organization, and movement is cell context-dependent.

RESULTS

Synthesized C13 modified cycloheximide analogues fluoresce with restricted rotation

Pioneering structural and biochemical studies have employed the natural product cycloheximide (CHX) (Fig. 1a) as a tool for deciphering ribosomal functioning,[33-35] based on CHX's selectivity and high affinity for eukaryotic ribosomes (Fig. 1b).[36] To enable live-cell imaging and tracking of ribosomes, we exploited CHX's privileged scaffold to develop ribosome-selective fluorescent probes (Fig. 1c). Specifically, previous studies showed that modifications at the glutarimide, C8 alcohol and C10 ketone of CHX diminish its binding affinity.[37, 38] The groups of Du Bois[39] and Liau[40] reported elegant synthetic routes to modify CHX at the C13 position instead, using C-H activation affording the C13 aminated analogue 2. Interestingly, derivatization at this position does not negatively affect ribosomal binding, which was speculated to be caused by additional stabilizing interactions within the binding pocket.[40] We therefore chose to append a fluorophore at this position to yield fluorescent probes.[41-44] The fluorescent rotor CCVJ was chosen as the fluorophore and three probes that differ in spacing between CHX and the fluorophore were prepared (Fig. 1d). The CCVJ molecular rotor has previously been reported to display increased emission when interacting with a biomolecular target,[45-49] which could provide additional resolution during live-cell imaging. We hypothesized that increased linker length could either be beneficial (by improving probe binding), or detrimental (by causing unperturbed rotation upon binding). Therefore, Probes 1-3 were synthesized by conjugating aminated analogue 2 with carboxylic acid-bearing CCVJ derivatives (Fig. 1d).

To assess if probes 1-3 retained CHX's biological activity, *in vitro* translation assays were performed. Binding of the probes to the ribosome would block translation of a luciferase-encoding mRNA, which can be measured spectroscopically. Probes 1-3 and CHX were incubated at increasing concentrations with the *in vitro* translation system and luminescence was measured (Fig. 1e). CHX displays an IC_{50} of 0.45 μM. Probes 1-3 show similar activity with IC_{50} values of 0.62 μM, 1.05 μM and 0.49 μM respectively, indicating that the conjugated fluorophore indeed does not substantially affect ribosomal binding, irrespective of linker length. Furthermore, Probes 1-3 display similar fluorescent properties (Supplementary Fig. 1a-b) with emission maxima at 500 nm in PBS (λ_{ex}=460 nm) (Fig. 1f, inset). To study the potentially increased emission and brightness (Supplementary Fig. 1e) in environments with altered viscosity and polarity, emission spectra were recorded in glycerol. Emission and quantum yields increase for all probes (Fig. 1f and Supplementary Fig. 1c-e) and minor shifts in emission maxima were observed, indicating responsiveness to altered environments.[50] Next, we assessed the performance of probes 1-3 in live human embryonic kidney (HEK293T/17) cells. When cells are incubated with probe 1, defined foci with enhanced fluorescence are observed throughout the cytoplasm (Fig. 1g-i). Interestingly, significantly weaker signal is detected for probe 2 and 3 (Fig. 1g-h). One explanation could be that the increased spacing between the CHX scaffold and the CCVJ rotor results in increased rotational freedom when bound to the target causing decreased emission.[50] Particularly, since the inherent fluorescence is similar for all probes (Fig. 1f). Based on these results, probe 1 was used for further experiments and dubbed RiboBright.

Sequencing and fluorescent imaging show that RiboBright binds the ribosome

To further verify that RiboBright binds ribosomes in cells, a cellular translation assay was performed. HEK293T/17 cells were pretreated with RiboBright or CHX and subsequently exposed to the puromycin analogue O-propargyl-puromycin (OPP) for 30 minutes, allowing for incorporation of OPP into newly synthesized proteins.[51] After fixation, the nascently translated polypeptides were fluorescently labelled with Alexa Fluor 647 using click chemistry and imaged (Supplementary Fig. 1f). As expected, with increasing concentrations of CHX and RiboBright, the incorporation of OPP into newly synthesized proteins decreases. This occurs more gradually for CHX than for RiboBright (Fig. 2a orange compared to blue). Notably, since RiboBright (similar to CHX) blocks translation, the probe's application is likely limited to ribosome visualization for shorter time periods (i.e., ideally within 30 minutes).

To determine if RiboBright retains affinity for the same binding pocket as CHX, a DMS-MaPseq experiment was performed.[52] To this end, HEK293T/17 cells were treated with RiboBright or CHX for 30 minutes and then exposed to 2% DMS. Cells treated with RiboBright or CHX show strong protection of C4341 (Fig. 2b).[53] The N-3 position of this cytosine forms a hydrogen bond with the C8 alcohol of CHX (Fig. 1b), protecting it from methylation by DMS.[40] In addition, co-staining in fixed cells with ribosomal antibodies reveals stronger colocalization of RiboBright with RPL7A (a 60S subunit marker) than with S6 (a 40S subunit marker), as quantified by the Manders coefficient (Supplementary Fig. 1g). These results suggest that RiboBright interacts with the same binding pocket as CHX. To further verify the selectivity of RiboBright towards the ribosomal E-site, we conducted cellular competition experiments. HEK293T/17 cells were pretreated with increasing concentrations of CHX for 30 minutes and then incubated with RiboBright and imaged immediately. Pretreated cells show a significantly lower signal compared to cells treated with RiboBright only (Fig. 2c) in a concentration-dependent manner (Supplementary Fig. 1g). These data confirm that the probe occupies the same binding pocket as CHX. To exclude off-target interactions that CHX and RiboBright could have in common due to their similar structure, we repeated this experiment with phyllantoside.[54] This structurally unrelated compound interacts with the same binding pocket as CHX.[54] Cells pretreated with phyllantoside for 30 minutes, exhibit only a weak fluorescent signal comparable to CHX pretreatment (Fig. 2c and Supplementary Fig. 1h), further validating the selective nature of the probe.

Next, organelle specific counterstains were applied to determine the cellular localization of RiboBright. Once the functional 80S ribosome is formed, it is present either as free-floating or bound to the endoplasmic reticulum (ER).[55] Furthermore, mitochondria contain their own ribosomes.[56] Therefore, cells were simultaneously incubated with RiboBright, along with ER (Fig. 2d, top) and mitochondrial (Fig. 2d, bottom) staining respectively. The degree of colocalization between RiboBright and the two respective stains was quantified using the Manders Coefficient. While both mitochondria and ER colocalize strongly with RiboBright (Fig. 2d, right; M2 - bottom), not all of RiboBright signal colocalizes with either of these two stains (Fig. 2d, right; M1 - top). Together, this analysis indicates that RiboBright binds to ribosomes in the ER as well as mitochondrial ribosomes. These findings are in line with literature evidence indicating that more ribosomes than originally anticipated undergo ER-localized translation.[57] Intuitively, however, not all of the RiboBright signal is associated with ER or mitochondrial ribosomes, likely representing free cytoplasmic ribosomes. Collectively, the sequencing results combined with fluorescent imaging data show that RiboBright selectively binds ribosomes.

RiboBright enables ribosome tracking in single cells

Having shown that RiboBright is selective for the ribosome, we next examined if the probe could be used to track ribosome movement. Cells were incubated with RiboBright and imaged with a frequency of 400 ms for 1 minute, enabling tracking of individual fluorescent foci (Fig. 3a and Supplementary Movie 1-4). Notably, this trajectory analysis did not include tracking in the Z direction, to avoid increasing the imaging frequency and therefore allow tracking of trajectories that move relatively quickly. Interestingly, when plotting the XY coordinates of fluorescent foci, they either display rapid movement with an apparent directionality (Fig. 3b and Supplementary Movie 1, pink, $\alpha \geq 1.2$ considered super diffusion), random movement (Fig. 3b and Supplementary Movie 2, light blue, $0.8 \leq \alpha \leq 1.2$ considered normal diffusion) or remain relatively stationary (Fig. 3b and Supplementary Movie 3, dark blue, $\alpha \leq 0.8$ considered confined diffusion). To classify each track by the dominant type of movement it displays, we first computed the mean squared displacement (MSD) at increasing time lags (Fig. 3c).[58] Specifically, a linear relationship ($\alpha \sim 1$) between the MSD and time lag indicates normal diffusion; confined diffusion resulting from steric barriers, crowding, or binding to cellular structures, is characterized by $\alpha \leq 0.8$; and super-diffusion caused by directed motion, typically exhibits $\alpha \geq 1.2$.[59] Notably, as previously described,[58] some foci transition between different behaviors (Fig. 3d). The Packing coefficient (Pc) can identify these transitions[60], as Pc values inversely scale with the area of confinement (Fig. 3d, bottom left). As expected, the instantaneous diffusion coefficient (D_i) calculated for the same time windows, decreases during the Brownian-defined periods (Fig. 3d, bottom right). While for such transitions α-estimation from MSD is a generalization, the dominant behavior of a track can still be estimated and the average MSD of all tracks shows good reproducibility between replicates (Fig. 3e, dashed and full line).

When quantifying the percentage of tracks displaying each type of diffusion (i.e., confined, normal, and super), most tracks reveal confined diffusive behavior (Fig. 3e, dark blue), likely representing a combination of ribosomes embedded in the ER, ribosomes translating mRNAs that are themselves tethered to organelles or cytoskeletal structures, or polysomes undergoing translation that are more likely to dwell locally.[29, 59, 61] Interestingly, there is high variability in diffusion coefficients within each category when comparing all measured tracks (Fig. 3f), as well as the average diffusion coefficient per single cell (Fig. 3g). Yet, the average diffusion coefficients over all tracks still show good reproducibility among replicates, both at a population level (Fig. 3f) and at a single-cell level (Fig. 3g). Average D is ~0.007 $\mu m^2 s^{-1}$, ~0.015 $\mu m^2 s^{-1}$ and ~0.029 $\mu m^2 s^{-1}$, for the confined, normal and super diffusive trajectories, respectively. This is within a comparable range as previous reported values of untethered (0.047 $\mu m^2 s^{-1}$) or tethered (0.0016 $\mu m^2 s^{-1}$) mRNAs associated with ribosomes,[62] and polysomes in the perinuclear region (0.0053 $\mu m^2 s^{-1}$) or not in the perinuclear region (0.028 $\mu m^2 s^{-1}$).[59] Collectively, these data demonstrate that RiboBright can be used to quantify ribosome movement in live cells.

RiboBright allows ribosome quantification across diverse cellular contexts

Having validated RiboBright in HEK293T/17, we next sought to apply it to study cell-line specific variations in ribosomal behavior. Specifically, we used mESCs, HCT 116, MCF 10A, SH-SY5Y, PC-9, HeLa, U2OS, SK-MEL-28, and PANC-1, together with HEK293T/17 cells (Fig. 4a and Supplementary Table 1). Interestingly, all human cell lines show similar fluorescent foci to the

ones observed in HEK293T/17 cells when stained with RiboBright, while undifferentiated mouse embryonic stem cells (mESCs) show fewer cytoplasmic RiboBright foci (Fig. 4a). The foci vary in size, intensity, and localization across cell types. The smaller foci, close to the diffraction limit, may represent single ribosomes or small assemblies, while the larger and brighter foci could reflect higher-order clusters, regions of increased ribosomal density or ribosome associated vesicles (RAVs).[63] Such heterogeneity in ribosome organization may relate to differences in subcellular compartmentalization. Although the precise nature of these structures remains to be determined, their diversity suggests cell type-specific modes of ribosome organization. Furthermore, these foci are unlikely to result from non-specific binding or fluorophore aggregation, as they are absent when probes with longer linker variants are used (Fig. 1g) and can be eliminated in two independent competition experiments (Fig. 2c). Notably, mESCs show a higher signal on the nuclear envelope. It is thought that ribosomes are more concentrated around the nuclear envelope during the G2 phase of their cell cycle[26] and mESCs have a longer S/G2/M than G1 phase,[64] potentially explaining why RiboBright is particularly apparent on the nuclear envelope for this cell type. Next, we sought to quantify total single-cell RiboBright signal of all 10 adherent (Fig. 4b and Supplementary Fig. 2a), as well as 2 additional suspension (Supplementary Fig. 2b), cell types by flow cytometry. While most cell types show clear unimodal distributions, human non-small cell lung carcinoma (PC9) cells show a tail of approximately 5.4% of cells that exhibit lower RiboBright signal. The Ribosome Biogenesis Regulator 1 (RBIS) is highly expressed in PC9 cells[65] and knockdown of RBIS substantially increased sensitivity of lung adenocarcinoma cells to chemotherapeutic drugs.[66] It is possible, that this subpopulation of low RiboBright cells, could therefore be more drug sensitive. When tracking RiboBright foci, cell-type specific differences in the diffusive behavior (Supplementary Fig. 2c) as well as diffusion coefficients for super, normal, and confined diffusion respectively (Supplementary Fig. 2d) emerge. Yet, both the diffusive behavior as well as diffusion coefficients do not show any clear trend with respect to cell size.

Knowing that the RiboBright staining can be used on various cellular models, we next sought to determine whether ribosome levels correlate with translation levels across different cell types. To this end, we incubated all cell types with the puromycin analogue O-propargyl-puromycin (OPP) for 30 minutes, allowing for its incorporation into newly synthesized proteins.[51] Following fixation, click chemistry was employed to label the newly synthesized proteins containing OPP and co-stained ribosomes with RiboBright (Fig 4c). Fixation reveals sub micrometer-sized foci (Supplementary Fig. 2e), which might be more difficult to visualize in live cells because they move faster than the exposure time. As expected, mitotic cells display very low translation levels while maintaining ribosome content (Fig. 4c, arrows).[67] Interestingly, larger RiboBright foci are less apparent in mitotic cells as previously observed by EM (Fig. 4c, arrows) supporting the idea that smaller foci represent individual ribosomes and larger foci may correspond to ribosomal clusters, polysomes, or RAVs.[63, 68] Next, the average fluorescence intensity of both OPP and RiboBright was quantified in the same cell at the single-cell level (Fig 4d and Supplementary Fig. 3a). While most cell lines show no correlation between translation levels and ribosome content, HeLa and SKMEL28 cells show a slight positive correlation (0.52 and 0.42 respectively). Some cancer cells such as human non-small cell lung carcinoma (PC9) cells and colon cancer (HCT116) cells show two populations: one with high and one with low translational activity. mESCs display the lowest variability (quantified as the Fano factor = σ^2/μ) in translation levels across the 10 analyzed cell lines (Fig. 4e, brown). Furthermore, a correlation between RiboBright intensity and variability in translation levels is visible across all cell lines (Fig. 4e). This is consistent with previous evidence

suggesting that variability in protein output can be minimized by low ribosome abundance.[69] Maintaining low ribosome abundance, might therefore provide cells with a mechanism to achieve constant global protein output in contexts where this is beneficial.

Both average RiboBright intensity and OPP intensity vary significantly across cell lines (Supplementary Fig. 3b-d) with no clear cell-size dependent trend (Supplementary Fig. 3c-f). We thus sought to quantify the per-ribosome translational efficiency in each cell type, which was defined as the translation levels per cell normalized by ribosome concentration (i.e., calculated as OPP intensity / RiboBright intensity per single cell). Some cell lines, such as PC9, show clear bimodality in per-ribosome translational efficiency across single cell (Supplementary Fig. 3g), and the undifferentiated cell line tested (mESCs) revealed the lowest per-ribosome translational efficiency (Fig. 4f). When quantifying the percentage of ribosomal tracks that are perinuclear (defined as a region within 1 μm of the nucleus), mESCs show the highest number of perinuclear tracks (Supplementary Fig. 3h). Furthermore, there appears a slight negative correlation with both OPP and RiboBright intensity. The low per-ribosome translational efficiency quantified for mESCs aligns with existing literature indicating that ribosome biogenesis in stem cells significantly exceeds translation levels compared to differentiated cells.[70-73] Although the underlying reasons for this phenomenon remains unclear, it appears that elevated ribosome levels may be necessary to sustain undifferentiated states in stem cells.[73]

Together, these data show the versatile nature of RiboBright, both with respect to cell lines (demonstrated in a total of 12 cell lines, both human and mouse) and analysis methods (both fixed and live cells, the latter measured by microscopy and flow cytometer).

RiboBright reveals lineage-specific ribosome behavior in differentiating mESCs

To investigate changes in ribosome levels and kinetics during differentiation, we applied RiboBright to differentiating mESCs, a well-characterized model system to study differentiation. Specifically, mESCs are derived from the inner cell mass of a mouse embryo and can differentiate into precursors of all three primary germ layers: ectoderm, endoderm and mesoderm.[74, 75] The differentiation of mESCs can be induced by switching from a leukemia inhibitory factor (LIF)-containing medium to a basal medium (NB27) supplemented with retinoic acid (RA). This differentiation is accompanied by a decrease in the pluripotency marker NANOG (Supplementary Fig. 4a). As previously described, in the presence of RA, mESCs can also differentiate into extraembryonic endoderm (XEN) cells and therefore undergo an early lineage decision to become ectoderm (ECT)-like or XEN-like (Fig. 5a).[76, 77] To distinguish between these differentiated cell types, we employed fluorescently labeled antibodies targeting the CD24 surface marker in the ectoderm-like cells, and the CD140a marker in XEN cells.[76, 77]

We combined the antibody staining with RiboBright and measured ribosome levels via flow cytometry 72 hours after differentiation induction. Interestingly, after the onset of differentiation both CD24+ as well as CD140a+ cells exhibit higher ribosome signal than CD24-/CD140a- cells (Fig. 5b-c and Supplementary Fig. 4b). Knowing that ribosome levels change in a lineage specific manner upon differentiation,[78] we next sought to quantify the average RiboBright signal per cell through microscopy, which reflects a proxy for ribosome concentration, and cells retain their

physiological shape and volume during imaging. Ectoderm-like (CD24+) cells show very slight elevated signal intensity compared to CD24– cells, whereas XEN (CD140a+) cells exhibit no significant difference in concentration (Fig. 5e). However, because XEN cells are larger (Fig. 5f), we also calculated the total ribosome signal per cell (intensity × cell area). By this measure, both CD24+ and CD140a+ cells display a slightly elevated total ribosome content relative to marker-negative cells (Supplementary Fig. 4c). These trends are consistent with flow cytometry data (Fig. 5b–c), though the fold-change in mean detected by flow cytometry is greater than the fold-change in mean observed by single-cell imaging. This could reflect differences in experimental conditions (detached versus adherent) or simply the larger number of replicates and cells analyzed in the flow cytometry experiments. At 72 hours the tracking of the cytoplasmic foci in the different cell types reveals that CD140a+ cells display the lowest diffusion coefficients (Fig. 5g), with the largest effect size and therefore also likely the most physiologically relevant. XEN cells tend to be morphologically distinct from ectoderm-like and double negative cells, with longer protrusions (Fig. 5d) and larger cell area (Fig. 5f and Supplementary Fig. 4c). Other elongated cell types, such as neuronal cells, exhibit localized translation,[79] possibly explaining the significantly lower diffusion coefficients for XEN cells. Supporting this argument, XEN (CD140a+) cells show slightly more confined ribosomal tracks than ectoderm-like (CD24+) and double-negative (CD24-/CD140a-) cells (Supplementary Fig. 4d). Lastly, neither CD24 nor CD140a signal correlates with RiboBright intensity (Supplementary Fig. 4e-f). Taken together, these data reveal a potential lineage-specific shift in ribosome biogenesis and movement.

RiboBright exposes large translationally active hubs unique to the ectoderm-like lineage

We next sought to determine how ribosome abundance and translation changes during the initial stages of differentiation.[80, 81] Early studies proposed that during differentiation the translation rate increases and ribosome biogenesis decreases.[82] These population-based studies found that ribosome loading and therefore translational efficiency of individual mRNAs is upregulated during differentiation.[83, 84] However, more recent literature suggests that translation regulation is highly dynamic throughout differentiation.[81, 85, 86] Our single-cell analysis reveals that undifferentiated mESCs have very low per-ribosome translational efficiency and no correlation between ribosome abundance and global translation (Fig. 4). Furthermore, we identify lineage-specific changes in ribosome content and movement (Fig. 5) already at early stages of differentiation. This led us to question whether the early onset of differentiation (24-72 hours) would be accompanied by changes in both ribosome content and translation levels. To this end, we co-stained differentiating mESCs with RiboBright and the OPP-assay employed previously (Fig. 4) at 24, 48, and 72 hours after initiation of differentiation (Fig. 6a). Interestingly, we observed translational hubs appearing after 48-72 hours of differentiation (Fig. 6a, RA), where both a very high RiboBright and OPP signal were present (Fig 6b). Because both CD24 and CD140 are surface markers and the OPP-assay requires fixation and permeabilization of cells, we were unable to distinguish between specific lineages. We therefore performed an additional analysis on the CD24/CD140a and RiboBright co-stained cells to determine the percentage of cells in each lineage that showed these RiboBright clusters at 72 hours into differentiation. To quantify cells containing RiboBright clusters of high intensity, we applied a threshold to the RiboBright signal (Supplementary Fig. 4g, pixel intensity > 4000 a.u.), categorizing cells as containing high RiboBright clusters if they contain pixels exceeded this threshold. Surprisingly, ~30% of ectoderm-like cells (CD24+) and

only ~15% of XEN (CD140a) cells and less than 10% double-negative (CD24-CD140a-) cells show these bright hubs, indicating that they are more specific to ectoderm-like cells (Fig. 6c).

We proceeded to investigate changes in ribosome content and translation over the first 72 hours of differentiation. We therefore quantified OPP and RiboBright signal in single cells at 24, 48 and 72 hours into differentiation and compared it to a control that remained in undifferentiated culture conditions (LIF) for the same amount of time. To account for any potential imaging differences, we computed Z-score normalized values for OPP and RiboBright intensities, as well as the $\log_2$-transformed OPP/RiboBright ratio, per time point. This normalization ensures that all comparisons reflect relative translational activity rather than absolute fluorescence intensity. Interestingly, both the normalized RiboBight and OPP signal at the single-cell level are slightly lower in differentiating mESCs compared to the LIF condition over the onset of differentiation (Supplementary Fig. 4h, top), reflecting possible relative changes in translational activity rather than absolute ribosome levels. This occurs as early as 24 hours into differentiation, even before lineage-specific markers of differentiation appear (Fig. 6d).[77] Notably, we found that in differentiation culture conditions, CD24+ and CD140a+ cells exhibit higher RiboBright signal than CD24-/CD140a- (Fig. 5), indicating that these cells are not truly undifferentiated and these differences represent lineage-specific changes. Conversely, the observed decrease in RiboBright signal when comparing LIF to RA culture conditions reflect a change in differentiation state of cells. As previously reported, under differentiating culture conditions, cells exhibit a significantly longer G1 phase, during which they initiate differentiation.[87] [88] Given that RiboBright signal correlates with the cell-cycle stage (Supplementary Fig. 4i), the observed decreases may, at least in part, reflect the higher proportion of G1-phase cells in differentiating culture conditions. One hypothesis that could reconcile these data, is that while global translation and ribosome content decreases (possibly due to cell-cycle differences), in individual cells the ribosomes that are present are more translationally active. This should result in an increased correlation between RiboBright and OPP signal, as well as an increase in per-ribosome translational efficiency in single cells. Indeed, the cells that have a higher ribosome content are also more translationally active, demonstrated by an increased correlation between RiboBright and OPP signal in the RA (differentiating) conditions compared to the LIF control (undifferentiated), 72 hours into differentiation (Fig. 6e-f). Furthermore, the per-ribosome translational efficiency of mESCs is slightly higher in RA conditions compared to LIF conditions as early as 48 hours into differentiation, which coincides with the appearance of translational hubs (Fig. 6e and Fig. 6a). Notably, these changes are slight, therefore likely not yet impacting cellular function, and instead may only become significant at later stages in differentiation. Finally, co-localization analysis shows that RiboBright-mitochondria co-localization changes more than RiboBright-ER co-localization, indicating that ribosome localization is dynamically remodeled during differentiation (Fig. 6g-h). Overall, these findings indicate that the localization of ribosomes and translation is lineage-specific, with ribosome abundance and global translation decreasing yet the relative per-ribosome translational efficiency increases slightly during early stages of differentiation.

DISCUSSION

Visualizing ribosomes in live cells remains a challenge due to their structural complexity and dynamic nature. These macromolecular machines exist in both free cytosolic and ER-bound forms, playing a central role in gene expression regulation. Given their heterogeneity and implications in

gene regulation, tracking ribosomes in real-time is crucial for understanding their spatiotemporal dynamics. To address this need, we developed RiboBright, a fluorescent probe derived from CHX, which binds selectively to the E-site of the ribosome. By modifying CHX with a fluorescent rotor (CCVJ), RiboBright emits fluorescence upon ribosome binding, allowing visualization with high selectivity (Fig. 1). Competitive binding assays and DMS-MaPseq confirm that RiboBright interacts with ribosomes in the same manner as CHX, making it a reliable tool for live-cell imaging of translation (Fig. 2). Live-cell tracking of RiboBright foci reveals diverse ribosomal movement patterns, including directed, random, and stationary behaviors (Fig. 3). Consistently across 10 cell types, the majority of tracked ribosomes exhibit confined diffusion, while only a subset displays super-diffusive behavior or active transport (Fig. 4). Therefore, RiboBright serves as an easy implementable tool to track ribosomes not only within cells, but potentially also to study the trafficking of ribosomes between cells.[89]

Beyond live-cell imaging, RiboBright also facilitates ribosome quantification in fixed cells, as well as through flow cytometry enabling broader applications in translational research (Fig. 4, Supplementary Table 2). Interestingly, ribosome content correlates with cell-to-cell variability in global translation levels, introducing the idea that ribosome biogenesis, might act as a global regulator of gene expression noise. The translation efficiency per ribosome varies significantly between cell lines, with mESCs exhibiting the lowest per-ribosome translational efficiency. This is consistent with undifferentiated mESCs relying on high numbers of latent ribosomes to maintain an undifferentiated state.[73] This per-ribosome translational efficiency subsequently increases within 48 hours of differentiation of mESCs (Fig. 6). Yet, both ribosome content and global translation decrease as early as 24 hours into differentiation, prior even to lineage-specific markers emerging, which could be due to cell-cycle changes.

RiboBright reveals translationally active hubs with high ribosome content, that are more apparent in the ectoderm-like lineage and appear 48 hours into differentiation (Fig. 6). Conversely, the XEN-lineage exhibits more stationary ribosomes and overall slower movement of ribosomes irrespective of the movement type (Fig. 5), consistent with their distinct morphology, including elongated protrusions. Such constrained movement patterns may reflect localized translation within specific subcellular regions, potentially supporting cell-type–specific functions such as secretory activity or signaling.[90, 91] The resemblance to neuronal cells, which exploit localized translation, further suggests that ribosome localization plays a key role during early stages of fate determination.[92, 93] In this view, the reduced mobility of ribosomes in XEN cells may promote spatially restricted protein synthesis. By contrast, the higher ribosome mobility observed in CD24+ ectoderm-like cells likely enables more dynamic translational responses, potentially facilitating cell-to-cell communication processes important for ectodermal lineage specification.[94, 95] Lineage-specific differences in ribosome dynamics may depend on cytoskeletal organization,[96, 97] cellular energy state (e.g., ATP availability),[82, 98] and interactions with RNA-binding proteins that regulate localized translation.[99, 100] In this context, ribosome movement appears to not only reflect cell identity but also contribute actively to the establishment of distinct functional programs during differentiation. Yet, future applications of RiboBright with other complementary single-cell approaches is needed to determine whether ribosome mobility passively reflects cell identity or actively shapes lineage-specific protein synthesis. Taken together, ribosome regulation throughout differentiation appears to be multilayered, yet has historically been challenging,[101] RiboBright

therefore will further facilitate these studies in future. Overall, RiboBright provides a versatile and accessible approach for investigating ribosome behavior in diverse physiological contexts.

METHODS

Quantum Yield Determination.
The quantum yield of probe **1** – RiboBright (See Supplementary Methods for Synthesis) – was determined following the method of Mchedlov-Petrossyan and coworkers[88] using aminofluorescein as a reference and the following equation:

$$\varphi(1) = \frac{Em(1)x\varphi(2)}{Em(2)}$$

$\varphi(1)$: Probe 1 quantum yield
Em(1): Probe 1 fluorescence at 460 nm excitation and 500 nm emission in water and 460 nm excitation and 510 nm in glycerol
$\varphi(2)$: 5-Aminofluorescein quantum yield from literature[102]
φ(water) = 0.008
φ(glycerol) = 0.1
Em(2): 5-Aminofluorescein fluorescence at 460 nm excitation and 500 nm emission and 460 nm excitation and 510 nm in glycerol.

In vitro translation assays.
The *in vitro* translation assays were performed using Flexi Rabbit Reticulocyte Lysate System, purchased from Promega Corporation. The assays were performed according to manufacturer's instructions in a total reaction mixture of 10 µL, containing 7 µL Flexi Rabbit Reticulocyte Lysate, 0.1 µL Amino Acid Mixture Minus Leucine, 0.1 µL Amino Acid Mixture Minus Methionine, 0.28 µL Potassium Chloride (2.5 M), 0.2 µL Milli-Q water, 0.2 µL Luciferase Control RNA (1 mg/mL), 1 µL Luciferase Assay Reagent and 1.12 µL control medium (in H_2O with 1.5% DMSO). The reaction mixtures were incubated at 30 °C for 4 hours while luminescence was being measured in real time. Each assay was performed in triplicates and the luminescence signal was measured using BioTek Synergy H1 Plate Reader.

Cell culture.
HEK293T/17 (ATCC), SH-SY5Y (Prof. Ger Pruijn, Radboud University), HeLa (Prof. Wilhelm Huck, Radboud University), U2OS (Dr. Klaas Mulder, Radboud University), PANC-1 (Prof. Rene Bernard, Netherlands Cancer Institute) and HCT 116 cells (Dr. Klaas Mulder, Radboud University) were cultured in Dulbecco's modified Eagle's medium (DMEM, ThermoFisher) supplemented with 4.5 g/L D-Glucose, L-glutamine, Sodium Pyruvate, 10% (v/v) fetal bovine serum (FBS, ThermoFisher) and antibiotic solution (50 U/mL Penicillin and 50 U/mL Streptomycin). mESC-E14 (mESCs) (129/Ola background) were obtained from Dr. Hendrik Marks, originally from ATCC, with RRID:CVCL_9108[103]. The Nanog-GFP knock-in cell line was generated from mESC-E14 (provided by Prof. Leor S. Weinberger) through Cas9 mediated homologous recombination of eGFP into the C terminus of the endogenous Nanog gene[104]. Both mESCs lines were cultured continuously without feeder layers and only on precoated 0.1% gelatin (Sigma Aldrich, 48723-500G). Cells were maintained undifferentiated in high glucose-Dulbecco's Modified Eagles Medium (Gibco™) supplemented with 15% fetal bovine serum (Gibco™), 2 mM L-glutamine (Gibco™), 1 mM sodium pyruvate (Gibco™), antibiotic solution (50 U/mL Penicillin and 50 U/mL Streptomycin), 0.1 mM beta-mercaptoethanol (Gibco™) and 500 U/mL recombinant leukemia inhibitory factor (LIF, Millipore). PC-9 cells were cultured in RPMI 1640 GlutaMAX medium supplemented with 10% (v/v) FBS and antibiotic solution (50 U/mL Penicillin and 50 µg/mL Streptomycin). SK-MEL-28 cells were cultured in DMEM supplemented with Hepes 10

mM, FBS 10% (v/v) and antibiotic solution (50 U/mL Penicillin and 50 µg/mL Streptomycin). MCF 10A (Dr. Wenny Peeters, RadboudUMC) were cultured in DMEM/F-12 (Nutrient Mixture F-12, Sigma-Aldrich) medium supplemented with 5% horse serum (Sigma-Aldrich), antibiotic solution (50 U/mL Penicillin and 50 µg/mL Streptomycin), 10 µg human EGF (Sigma-Aldrich), 5 mg insulin (Sigma-Aldrich), 0.05 mg Cholera Toxin (Sigma-Aldrich), 1 mM Dexamethasone (Sigma-Aldrich).
All cell lines were incubated at 37°C, in a humified 5% CO2 atmosphere, until reaching a confluency of 70-80%.

DMS-MaPseq.
HEK293T/17 cells were seeded at a concentration of $1x10^5$ cells/mL in a 6-well plate two days prior treatment. At the moment of treatment, the culture medium was replaced with warm complete DMEM supplemented with 10 µM probe, 10 µM CHX or an equivalent volume of DMSO. Cells were incubated with the respective molecule for 30 minutes at 37°C. A final concentration of 2% of DMS was added directly to the wells and cells were incubated for exactly 4 minutes at 37°C. Medium was discarded and cells were washed with fresh Wash Buffer (60% v/v PBS 1x, 40% v/v β-mercaptoethanol). Cells were collected, washed once with PBS 1x and centrifuged at 500 g for 4 minutes at RT. The cell pellet was lysed using TRIzol reagent and incubated at RT for 5 minutes. Subsequently, 0.5 volume of chloroform was added to the cell lysate. Samples were centrifuged for 15 minutes, at 12000 g at 4°C. The aqueous phase was transferred to clean tubes. RNA was then purified using the Zymo® Research Clean & Concentrator-5 kit, as per manufacturer's instructions. RNA was eluted in 15 µL nuclease-free water (NF water). Total RNA quality was assessed by capillary electrophoresis (Bioanalyzer, Agilent RNA 6000 Nano Kit).

The probed RNA was reverse transcribed using TGIRT-IIITM Reverse transcriptase. Briefly, to 5 µL of probed RNA, 1 µL of 5X Reverse Transcription buffer (250 mM Tris-HCl pH 8.3; 375 mM KCl; 15 mM MgCl2), 0.5 µL of random hexamers (10 µM) and 0.5 µL of dNTPs (10 mM) was added. The mixture was incubated for 8 min at 98 °C, to simultaneously fragment and denature the RNA, and immediately transferred to ice. Sample was supplemented with 0.25 µL of SUPERaseIn (20 U/µL), 0.25 µL DTT (0.1 M) and 0.25 µL TGIRT-IIITM Reverse transcriptase (200 U/L). Reverse transcription was carried out at typical conditions (25 °C 10 min, 57 °C 2 hours, hold 4 °C). Then, 1 µL of ice-cold proteinase K (1 µg/µL) was added to each sample, to degrade the reverse-transcriptase. Reaction was carried out at 37 °C for 20 minutes. Proteinase K was deactivated by adding 1 µL proteinase inhibitor cocktail (Sigma Aldrich, cat. P186; 1:2 dilution in water). Second strand synthesis was carried out using the NEBNext® Ultra IITM Non-Directional RNA Second Strand Synthesis kit (New England Biolabs, cat. E6111). Whilst on ice, 2 µL of NEBNext® UltraIITM Second Strand Synthesis reaction buffer, 1 µL of NEBNext® Ultra IITM second strand synthesis enzyme mix and 11 µL of nuclease-free water were added to the sample. The reaction was carried out as per manufacturer instructions. The resulting DNA was cleaned by adding 72 µL NucleoMagTM NGS Clean-up and Size Select beads (Macherey-Nagel), eluting in 12.5µL NF water. The eluted dsDNA was then used as input for the KAPA Hyperprep kit with Library amplification from Roche (cat. No. 07962363001). Sequencing was carried out on an Illumina NextSeq 2000 system with a P2 100 cycle flow cell.

All sequencing data was analyzed using the RNA-framework.[105] Briefly reads were aligned to Human Ribosomal RNA recovered from the RNA central Database (Accession codes:

URS0000726FAB and URS000075EC78): "*rf-map -mp "-–very-sensitive-local" -cmn 0 -ctn -cq5 20 -b2 -ow –bi*". Briefly *-mp* enables soft-clipping during alignment. Commands *-ctn* and *-ctm* remove reads with or trims ambiguously called bases. -cq5 trims all bases with phred quality lower than 20 on the 5' end. Mutations were counted with: "*rf-count -m -es -ni -nd -na*". This counts the mutations, whilst ignoring all insertions, deletions and ambiguously mapped segments and ensuring that nucleotides neighboring the mutation are above 20 in quality. Mutation rates were calculated using rf-norm, ignoring G and T bases and setting minimum coverage to 400: *"rf-norm -nm 1 -n 400 -rb AC -ni -sm 4".* Mutation rate was calculated as reported by Rouskin and coworkers,[5352] and normalized with 2-8% normalization.

RiboBright probe staining for image acquisition.
HEK293T/17 cells were seeded at 3.5 × 10^5 cells/mL in ibiTreat 8-well #1.5 polymer coverslips (Ibidi) pre-coated with 0.01% Poly-L-Lysine (Sigma-Aldrich). The following day, the culture medium was replaced with warm complete DMEM containing RiboBright probes at the desired final concentration, or an equivalent volume of DMSO for negative controls.
For the competition assay, cells were pre-treated for 30 min with cycloheximide (CHX; Sigma-Aldrich) or phyllanthoside (Biosynth), followed by direct addition of RiboBright probe to a final concentration of 10 μM. Images were acquired exactly 1 min after probe addition.

Translation blocking and protein synthesis assay.
The retained ability of the probe to block translation was tested using Click-iT™ Plus OPP Alexa Fluor™ 647 Protein Synthesis Assay Kit. HEK293T/17 cells were seeded at a concentration of $3.5x10^5$ cells/mL in an ibiTreat 8-well #1.5 polymer coverslips (Ibidi) previously coated with Poly-L-Lysine 0.01% (Sigma-Aldrich). The day after, medium was replaced with warm complete DMEM containing the probes or CHX at the final desired concentration, or an equivalent volume of DMSO. After 30 minutes of incubation at 37°C, medium was replaced with warm complete DMEM containing 20 μM Click-iT® OPP reagent and the same drug used in the pre-incubation step. Cells were incubated for 30 minutes at 37°C, then fixed using PBS in 4% formaldehyde and permeabilized with 0.5% Triton X-100. Fresh Click-iT® OPP Reaction Buffer Additive was prepared by diluting the 10X solution 1:10 in deionized water. A Click-iT® Plus OPP reaction cocktail was prepared by mixing Click-iT® OPP Reaction Buffer, Copper Protectant, Alexa Fluor® picolyl azide and Click-iT® OPP Reaction Buffer Additive. Cells were washed once with PBS, the reaction cocktail was added to each well and incubated for 30 minutes at room temperature, protected from light. The solution was removed and cells were rinsed once with of Click-iT® Reaction Rinse Buffer. Samples were washed twice with PBS and were ready for imaging.

For co-staining with RiboBright and OPP, the culture medium was replaced with medium containing 20 μM Click-iT® OPP reagent, and cells were incubated for 30 minutes at 37 °C. Cells from different lines (Figures 4d–f and S3a–f) were then fixed with 4% formaldehyde. For the mESC differentiation assay (Figures 6e and S4h), mESCs were fixed with 4% formaldehyde at the indicated time points during differentiation, as described in the Methods – Differentiation section. All samples were permeabilized with 0.5% Triton X-100 and processed using the Click reaction protocol described above. Following incubation and washing, cells were stained with 10 μM RiboBright in PBS and imaged immediately.

Immunostaining.
mESCs were seeded at a density of $3.5x10^5$ cells/mL into ibiTreat 8-well #1.5 polymer coverslips (Ibidi), previously coated with 0.1% gelatin (Sigma Aldrich, 48723-500G). The following day, cells were fixed with 4% formaldehyde and permeabilized with 0.5% Triton X-100. After blocking with 3% BSA for 1-hour at room temperature, primary antibodies --- S6 Recombinant Rabbit Monoclonal Antibody (9H8L2) (Invitrogen, 749 Catalog # 701374, RRID AB_2532476), RPL7A Polyclonal antibody (ribosomal protein L7a, AG7543, Proteintech, Catalog # 15340-1-AP) --- were diluted 1:100 in blocking buffer and incubated overnight at 4 °C. The next day, cells were washed with 1xPBS and incubated secondary antibodies: anti-mouse Alexa Fluor™ 647 (Invitrogen, Catalog #A-21236) and anti-rabbit Alexa Fluor™ 546 (Invitrogen, Catalog # A10040); 1:500 dilution in PBS) for 1 hour at room temperature. After subsequent washes, cells were incubated with 10 μM RiboBright in PBS and imaged immediately.

ER/mitochondrial and RiboBright probe staining for image acquisition.
Cells were seeded at 3.5 × 10^5 cells/mL in ibiTreat 8-well #1.5 polymer coverslips (Ibidi) pre-coated with 0.01% Poly-L-Lysine (Sigma-Aldrich) for HEK293T/17 cells or 0.1% gelatin (Sigma-Aldrich, 48723-500G) for mESCs.
For HEK293T/17 cells, the day after seeding, the culture medium was replaced with warm complete DMEM containing probes at the desired final concentration, or an equivalent volume of DMSO for negative controls. For mESCs, the culture medium was replaced with differentiation medium (see Differentiation of mESCs section).
After 72 h of differentiation, cells were incubated at 37 °C for 30 min in either Hank's Balanced Salt Solution (ThermoFisher) containing 1 μM ER-Tracker (ThermoFisher) or complete medium containing 200 nM MitoTracker (ThermoFisher). Following incubation, the staining solution was replaced with complete medium containing RiboBright probe at a final concentration of 10 μM. Samples were immediately imaged after probe addition.

Time lapse acquisition
Time lapses of HEK293T/17 cells stained with 10 μM probe were acquired with an NL5+ line-scanning confocal on an Olympus IX83 microscope equipped with a Prime BSI Express sCMOS camera, using a 100x/1.40 NA oil objective, in a temperature and CO_2 controlled chamber. Samples were excited with a 405 nm laser at 25% power with emission collected at 525 nm, and with 200 ms of exposure time. Images were captured at intervals of 400 ms over a duration of 1 minute.

RiboBright detection via flow cytometry.
HEK293T/17, mESCs, HCT 116, MCF 10A, SH-SY5Y, PC-9, HeLa, U2OS, SK-MEL-28, PANC-1, Jurkat and K562 cells were collected and diluted to a concentration of $1x10^6$ cells/mL in phenol red free media, containing 10 μM probe. Cells were incubated in a pre-heated water bath at 37°C for 30 minutes and gently agitated every 15 minutes. After incubation, flow cytometry analysis of the probe signal was performed in a BD FACSCalibur Flow cytometer. RiboBright signal was measured by 405 nm violet laser. Data analysis was performed with BD Flowjo.

Differentiation of mESCs.

The differentiation media consisted of 50% Neurobasal Medium NB27 (Gibco™) and 50% DMEM/F12 (Capricorn Scientific), supplemented with 2 mM L-glutamine (Thermo Scientific), 10 mM β-mercaptoethanol (Fisher Scientific), 1x N2 (Gibco), 1x B27 (Gibco), and with or without 0.25 μM retinoic acid (Sigma-Aldrich). The differentiation assay was typically conducted over a 72-hour period.

Immunostaining of differentiated mESCs.
Flow Cytometry: Differentiated mESCs were stained with PE anti-mouse CD24 antibody (BioLegend, Clone: 30-F1, Cat# 138504, RRID: AB_10578416), APC anti-mouse CD140a antibody (BioLegend, Clone: APA5, Cat# 135908, RRID: AB_2043970), along with their respective isotype controls (PE Rat IgG2c κ, Clone: RTK4174, Cat#400707, RRID: AB_326573; APC Rat IgG2a κ, Clone: RTK2758, Cat#400512, RRID: AB_2814702, BioLegend). Antibodies were added independently at final concentrations of 0.5 μg/mL (CD24) and 0.2 μg/mL (CD140a) in fresh differentiation medium. After incubation, cells were detached using Accutase™ (STEMCELL™ Technologies, Cat#07920), pelleted, and resuspended in phenol red–free medium containing 10 μM RiboBright. Cells were incubated in a 37 °C water bath for 30 minutes with gentle agitation every 15 minutes, then kept on ice until flow cytometry analysis.

For differentiation validation, NANOG-GFP mESCs were assessed by live-cell staining with Alexa Fluor® 647 anti-mouse CD24 (BioLegend, Clone: M1/69, Cat. No. 101818, RRID: AB_493484), Brilliant Violet 421™ anti-mouse CD140a (BioLegend, Clone: APA5, Cat. No. 135923, RRID: AB_2814036) and their corresponding isotype controls (Alexa Fluor® 647 Rat IgG2b, κ, Clone: RTK4530, BioLegend, Cat#400626, RRID: AB_389343; Brilliant Violet 421™ Rat IgG2a, κ, Clone: RTK2758, BioLegend, Cat#400536, RRID: AB_10959325) at 37 °C for 30 minutes with final concentrations of 0.5 μg/mL and 0.2 μg/mL, respectively. Isotype controls (Alexa Fluor® 647 Rat IgG2b, κ, BioLegend, Cat#400626; Brilliant Violet 421™ Rat IgG2a, κ, BioLegend, Cat#400536) were used for gating CD24+ and CD140a+ populations. Staining and measurement were followed by the same procedure described above.

Confocal Microscopy: Differentiated mESCs were stained with PE anti-mouse CD24 antibody (BioLegend, Clone: 30-F1, Cat# 138504, RRID: AB_10578416), APC anti-mouse CD140a antibody (BioLegend, Clone: APA5, Cat# 135908, RRID: AB_2043970), along with their respective isotype controls (PE Rat IgG2c κ, Clone: RTK4174, Cat#400707, RRID: AB_326573; APC Rat IgG2a κ, Clone: RTK2758, Cat#400512, RRID: AB_2814702, BioLegend) at final concentrations of 0.5 μg/mL and 0.2 μg/mL, respectively, in fresh differentiation medium. After staining, the medium was replaced with fresh medium containing 10 μM RiboBright, and cells were imaged immediately.

Image acquisition.
Live and fixed cells were imaged with an NL5+ line-scanning confocal on an Olympus IX83 microscope equipped with a Prime BSI Express sCMOS camera, using a 60x/1.42 NA, and a 100x/1.40 NA oil objective.
For all the experiment, the probes were excited using a 405 nm laser at 25-40% power with an exposure time of 300 ms. For the translation blocking and nascent protein synthesis (OPP) assays, OPP signal—reflecting newly synthesized proteins—was excited using a 647 nm laser at 17% power, with 300 ms exposure. Images were acquired either as z-stacks with 1.8 μm intervals or as

single z-planes for differentiated mESCs. For organelle labeling, ER and mitochondria were excited using 561 nm (50% power) and 640 nm (20% power) lasers, respectively, with 300 ms exposure per channel. Z-stacks were acquired at 0.5 μm steps. For differentiation assay, CD24 and CD140a were excited using a 546 nm laser at 80% power and a 647 nm laser at 30% power, respectively. These images were acquired as single z-plane. For RPL7A and S6 immunostaining, fluorescence signals were collected as z-stacks (0.5 μm step size) with 200 ms exposure. Excitation was performed using 561 nm (20% power) for RPL7A and 640 nm (60% power) for S6.

Image analysis - Manders coefficients:
To quantify co-localization between RiboBright (RB) and the target compartment (ER or mitochondria) in 3D, Manders' coefficients (M1, M2) were computed on the entire 3D image stack for each field of view. For each image, a single Otsu threshold per channel was computed from the full-stack intensity histogram and evaluated Manders' coefficients on the union domain of above-threshold voxels, Domain: $D = \{I_{\mathrm{RB}} > T_{\mathrm{RB}}\} \cup \{I_{\mathrm{Target}} > T_{\mathrm{Target}}\}$. Thus,

$$M1 = \frac{\sum I_{\mathrm{RB}}\,[I_{\mathrm{Target}} > T_{\mathrm{Target}}]}{\sum I_{\mathrm{RB}}\,[D]},\quad M2 = \frac{\sum I_{\mathrm{Target}}\,[I_{\mathrm{RB}} > T_{\mathrm{RB}}]}{\sum I_{\mathrm{Target}}[D]}$$

A single M1 and M2 value was reported for each image. When significance testing was required, we applied a PSF-aware 3D block-shuffle permutation: one channel (RB or the target) was randomized by permuting PSF-sized tiles, preserving within-tile structure while disrupting inter-channel alignment. For each image, the observed 3D Manders values were compared to a null distribution generated by these permutations; we report one-tailed permutation p-values and the 95th percentile of the null (the Manders value exceeded by only 5% of randomized runs). In our dataset, p-values were at the permutation limit (e.g., $p \leq 0.0078$ with 128 effective permutations), indicating that observed co-localization exceeded every randomized replicate and is therefore unlikely to arise by chance.
Data from multiple experiments, conditions (LIF and RA), markers (ER and Mito), replicates, and imaging views were aggregated for analysis.

Image analysis - Cell Segmentation.
Cell masks for single-cell analysis were generated using the deep-learning-based segmentation algorithm Cellpose 2D (implemented via the Cellpose_2D_ZeroCostDL4Mic.ipynb notebook from the ZeroCostDL4Mic suite; GitHub: https://github.com/HenriquesLab/ZeroCostDL4Mic). The default pre-trained Cellpose model (cyto or nuclei, as appropriate) was applied without additional training. Segmentation was performed using either the probe signal (cytoplasmic segmentation), differentiation markers (CD24 and CD140a, cytoplasmic segmentation), or OPP signal (nuclear segmentation) as input. Inference parameters were set as follows: flow_threshold = 0.98; mask_threshold = –0.55; estimated object diameters: 150 px (nuclear) and 200–250 px (cytoplasmic). For each segmented ROI, fluorescence intensity was quantified under identical acquisition conditions (laser power, detector gain, pinhole size, and dwell time held constant across samples). Pixels within the mask were background-corrected by subtracting the local background measured in adjacent cell-free regions. Both mean intensity (background-corrected fluorescence per unit area, reflecting concentration) and integrated density (mean intensity × ROI area, reflecting total abundance) were computed using in-house Python scripts.

Image analysis - Cell Volume Quantification.
For different cell lines (related to Fig. 4d–f and Supplementary Fig. 3a–f), cell volumes were determined from z-stacks. Each z-plane was binarized by thresholding to separate signal from background, and single-cell masks were projected across z. Masked regions were overlaid with binarized slices to extract cell-associated pixel areas. Volumes were computed by summing pixel areas across z and multiplying by the known step size.

Image analysis - Normalization for Differentiation Assay.
For mESC differentiation assays (related to Fig. 6e and Supplementary Fig. 4h), single-cell OPP and RiboBright intensities were measured as above. To account for differences in cell size and baseline translation activity, the intensity of RiboBright and OPP, as well as the ratio of OPP to RiboBright, were computed per cell and $\log_2$-transformed. To enable comparison across conditions, values (RiboBright, OPP, and $\log_2$-transformed ratios) were Z-score normalized per time point (subtracting the mean and dividing by the standard deviation of all cells within the time point).

Image analysis - Time lapse tracking analysis.
Image preprocessing was performed using Fiji[106] (ImageJ, version2.16). For each image sequence, the raw time-lapse stacks were first subjected to background subtraction using the built-in "Subtract Background" function (rolling ball radius = 90 pixels, "sliding paraboloid" option disabled, "light background" unchecked). Subsequently, the images were processed using the "Median..." filter (radius = 1 pixel) to reduce noise while preserving edge information. These steps were applied uniformly across all datasets prior to particle tracking. Fluorescent signals were tracked in Trackmate (TrackMate (imagej.net))[107] using the Nearest-neighbor tracker. Particles were detected using the LoG detector, with an estimated object diameter of 0.7 µm, and a quality threshold of 1.77. The maximal linking distance for the nearest-neighbor tracker was 0.8 µm. To filter out incorrectly tracked foci, additional filters were added to the tracks. Tracks consisting of fewer than 20 timepoints, having a linearity of forward progression > 0.63, and a mean quality < 4.50 were omitted from the analysis. Tracks were defined as perinuclear/nuclear at a single-cell level, where the perinuclear region was defined as an area of 1 µm around the nucleus. All remaining tracks were defined as peripheral.

For each track the MSD was computed using the equation (1):

$$MSD(\Delta t\tau) = \frac{1}{N-\tau}\sum_{i=0}^{N-\tau-1}(x_{i+\tau}-x_i)^2 + (y_{i+\tau}-y_i)^2 \quad (1)$$

where Δt is the time interval between two successive frames, τ represents the number of lag times, N is the total number of timepoints, and (x_i,y_i) denote the spatial coordinates at time i. The time dependence of the MSD, described by the equation (2) was used to classify each track into the different types of diffusional behavior:

$$MSD(t) = 4D\Delta t\tau^{\alpha} \quad (2)$$

where D denotes the diffusion coefficient, α represents the anomalous diffusion exponent. Employing nonlinear curve fitting, α was estimated from the MSD data. Tracks were categorized based on their α values as follows: $\alpha \leq 0.8$ denoted confined diffusion, $\alpha \geq 1.2$ signified super-

diffusion, and values falling in between were classified as normal diffusion. The diffusion coefficient (D) was computed for each MSD value of the same track using the equation (3):

$$D = \frac{\mathrm{MSD}}{4\Delta t\tau} \quad (3)$$

Subsequently, the average diffusion coefficient across all MSD values of the same track was calculated.

For single cell analysis, cell masks were obtained as described above, and the tracks were assigned to each mask based on their coordinates.

The packing coefficient (Pc) at each time point i was calculated as described by Renner et al.[60] using the following equation (4):

$$Pc_{\mathrm{i}} = \sum_{\mathrm{ji=i}}^{\mathrm{i+n-1}} \frac{\left(x_{ji+1} - x_{ji}\right)^2 + \left(y_{ji+1} - y_{ji}\right)^2}{S_{\mathrm{i}}^2} \quad (4)$$

Where (x_j,y_j) are the spatial coordinates at time j, n is the length of the time window (n=10), and S_i is the surface area of the convex hull of the trajectory segment between time points i and i+n. The value S_i was calculated using the ConvexHull function in SciPy, Python.[108] The corresponding instantaneous diffusion coefficients (D_{inst}) were calculated on the same time window, using the following equations (5, 6):

$$\text{Squared Displacement} = \sum_{\mathrm{i=0}}^{i+n-1} (x_{i+1} - x_i)^2 + (y_{i+1} - y_i)^2 \quad (5)$$

$$D_{inst} = \frac{\text{Squared Displacement}}{4\Delta tn} \quad (6)$$

Quantitative fluorescence analysis and marker-based cell classifications.

To quantify single-cell RiboBright fluorescence and nascent protein synthesis (via OPP labeling), two-channel fluorescence images were analyzed using a custom Python-based cell segmentation and quantification pipeline. For each field of view, RiboBright and OPP intensity images were aligned with pre-generated binary cell masks, from which we extracted mean intensity, total fluorescence, and cell area (derived from the RiboBright mask) for individual cells.

To account for inter-sample variability, single-cell RiboBright and OPP intensities at 24 h, 48 h, and 72 h were normalized relative to internal controls at each time point using z-score normalization: Normalized Intensity = $(X - \mu) / \sigma$, where X is the intensity of an individual cell, μ is the mean intensity of all cells within the same time point and channel, and σ is the corresponding standard deviation.

To quantify single-cell RiboBright fluorescence in differentiated mESCs, three-channel fluorescence images were analyzed using a custom Python-based segmentation and quantification pipeline. For each field of view, segmented masks for RiboBright, CD24, and CD140a were first filtered to exclude artifacts based on the following criteria: minimum area (>8000 px²), roundness (0.25–0.75), and exclusion of objects touching image borders. For each accepted cell, RiboBright signal was quantified as mean fluorescence intensity, total fluorescence (mean × area), and cell area. CD24 and CD140a expression were evaluated as mean intensity within the corresponding segmented region, and cells were retained only if expression exceeded channel-specific thresholds (CD24 ≥ 200; CD140a ≥ 150).

To classify cell types, each RiboBright-positive cell was assigned to one of four categories based on ≥ 90% spatial overlap with the CD24 and/or CD140a masks: CD24+, CD140a+, CD24+CD140a+ (double-positive), or CD24-CD140a- (double-negative).
Cells were mutually exclusively assigned to a single category based on these criteria. Importantly, no cell was counted in more than one category.

To identify high-intensity RiboBright hubs, RiboBright fluorescence images were first filtered using a fixed pixel intensity cutoff of 4000 (gray value) and a minimum area of 100 pixels to define High RB+ region. A cell was classified as High RB+ if any portion of its segmented CD24+ or CD140a+ region overlapped with a High RB+ region.

Cell cycle and RiboBright assay.
Mouse embryonic stem cells (mESCs) were seeded at 16,800 cells/mL in 24-well plates pre-coated with 0.1% gelatin (Sigma-Aldrich, 48723-500G). After 24 h, cells were detached using Accutase™ (STEMCELL Technologies, Cat#07920), pelleted by centrifugation, and resuspended in phenol red–free medium containing 10 μM RiboBright and 2 μL Hoechst 33342 (1 mg/mL stock, Merck, Cat#94403-1ML). Cells were incubated at 37 °C in a pre-heated water bath for 30 min with gentle agitation every 15 min. Following incubation, samples were kept on ice until analysis by flow cytometry. Hoechst fluorescence was detected in the DAPI channel, and RiboBright fluorescence in the GFP channel.

Quantification and statistical analysis.
Statistical comparisons between experimental conditions were carried out using the Mann–Whitney U test for non-parametric distributional comparisons (e.g., violin and boxen plots) and the Welch's t-test for mean comparisons (e.g., bar plots). Data were visualized with plots that overlay individual data points to display both distribution and variability. Fold changes (median or mean) and p-values are reported to reflect both effect magnitude and significance. Details regarding the number of replicates, specific statistical tests, and significance thresholds are provided in the relevant method sections and figure legends. Most statistical analysis have been performed in Python 3,[109] with SciPy[108] as the main package for statistical analysis. Graphical representations of statistical analysis are performed in Python 3 with matplotlib[110] and seaborn.[110, 111] Statistical experimental details can be found in the relevant figure legends.

DATA AVAILABILITY

All relevant data supporting the key findings of this study are available within the article and its Supplementary Information files. Due to the large number of images taken, these files, as well as any additional information needed to reanalyze the data, are available from the lead contact upon request. MaPseq sequencing data have been deposited at Gene Expression Omnibus (GEO) and are publicly available as of the date of publication at GSE316112 [https://www.ncbi.nlm.nih.gov/geo/query/acc.cgi?acc=GSE316112].

CODE AVAILABILITY

All code is publicly available on GitHub at https://github.com/XinyuHuRU/RiboBright-project.git.

References

1. Bohnsack, K.E. & Bohnsack, M.T. Uncovering the assembly pathway of human ribosomes and its emerging links to disease. *EMBO J* **38**, e100278 (2019).
2. Ozadam, H. *et al.* Single-cell quantification of ribosome occupancy in early mouse development. *Nature* **618**, 1057–1064 (2023).
3. VanInsberghe, M., van den Berg, J., Andersson-Rolf, A., Clevers, H. & van Oudenaarden, A. Single-cell Ribo-seq reveals cell cycle-dependent translational pausing. *Nature* **597**, 561–565 (2021).
4. Zeng, H. *et al.* Spatially resolved single-cell translatomics at molecular resolution. *Science* **380**, eadd3067 (2023).
5. Brenner, S., Jacob, F. & Meselson, M. An unstable intermediate carrying information from genes to ribosomes for protein synthesis. *Nature* **190**, 576–581 (1961).
6. Samir, P. *et al.* Identification of Changing Ribosome Protein Compositions using Mass Spectrometry. *Proteomics* **18**, e1800217 (2018).
7. Jouffe, C. *et al.* The circadian clock coordinates ribosome biogenesis. *PLoS Biol* **11**, e1001455 (2013).
8. Sinturel, F. *et al.* Diurnal Oscillations in Liver Mass and Cell Size Accompany Ribosome Assembly Cycles. *Cell* **169**, 651–663 e614 (2017).
9. Wu, B., Eliscovich, C., Yoon, Y.J. & Singer, R.H. Translation dynamics of single mRNAs in live cells and neurons. *Science* **352**, 1430–1435 (2016).
10. Dalla Venezia, N., Vincent, A., Marcel, V., Catez, F. & Diaz, J.J. Emerging Role of Eukaryote Ribosomes in Translational Control. *Int J Mol Sci* **20** (2019).
11. Joo, M. *et al.* Specialised ribosomes as versatile regulators of gene expression. *RNA Biol* **19**, 1103–1114 (2022).
12. Brombin, A., Joly, J.S. & Jamen, F. New tricks for an old dog: ribosome biogenesis contributes to stem cell homeostasis. *Curr Opin Genet Dev* **34**, 61–70 (2015).
13. Ruggero, D. Translational control in cancer etiology. *Cold Spring Harb Perspect Biol* **5** (2013).
14. White, R.J. RNA polymerases I and III, non-coding RNAs and cancer. *Trends Genet* **24**, 622–629 (2008).
15. Drygin, D., Rice, W.G. & Grummt, I. The RNA polymerase I transcription machinery: an emerging target for the treatment of cancer. *Annu Rev Pharmacol Toxicol* **50**, 131–156 (2010).

16. Bustelo, X.R. & Dosil, M. Ribosome biogenesis and cancer: basic and translational challenges. *Curr Opin Genet Dev* **48**, 22–29 (2018).
17. Ingolia, N.T., Hussmann, J.A. & Weissman, J.S. Ribosome Profiling: Global Views of Translation. *Cold Spring Harb Perspect Biol* **11** (2019).
18. Brar, G.A. & Weissman, J.S. Ribosome profiling reveals the what, when, where and how of protein synthesis. *Nat Rev Mol Cell Biol* **16**, 651–664 (2015).
19. Schwanhausser, B. *et al.* Global quantification of mammalian gene expression control. *Nature* **473**, 337–342 (2011).
20. Saady, A., Varon, E., Jacob, A., Shav-Tal, Y. & Fischer, B. Applying styryl quinolinium fluorescent probes for imaging of ribosomal RNA in living cells. *Dyes and Pigments* **174**, 107986 (2020).
21. Cao, C. *et al.* Ribosomal RNA-Selective Light-Up Fluorescent Probe for Rapidly Imaging the Nucleolus in Live Cells. *ACS Sens* **4**, 1409–1416 (2019).
22. Burke, K.S., Antilla, K.A. & Tirrell, D.A. A Fluorescence in Situ Hybridization Method To Quantify mRNA Translation by Visualizing Ribosome-mRNA Interactions in Single Cells. *ACS Cent Sci* **3**, 425–433 (2017).
23. Ignacio, B.J. *et al.* THRONCAT: metabolic labeling of newly synthesized proteins using a bioorthogonal threonine analog. *Nat Commun* **14**, 3367 (2023).
24. Dieterich, D.C., Link, A.J., Graumann, J., Tirrell, D.A. & Schuman, E.M. Selective identification of newly synthesized proteins in mammalian cells using bioorthogonal noncanonical amino acid tagging (BONCAT). *Proc Natl Acad Sci U S A* **103**, 9482–9487 (2006).
25. Bastide, A., Yewdell, J.W. & David, A. The RiboPuromycylation Method (RPM): an Immunofluorescence Technique to Map Translation Sites at the Sub-cellular Level. *Bio Protoc* **8** (2018).
26. Tsai, Y.J., Lee, H.I. & Lin, A. Ribosome distribution in HeLa cells during the cell cycle. *PLoS One* **7**, e32820 (2012).
27. Shore, D. & Albert, B. Ribosome biogenesis and the cellular energy economy. *Curr Biol* **32**, R611–R617 (2022).
28. Metelev, M. *et al.* Direct measurements of mRNA translation kinetics in living cells. *Nat Commun* **13**, 1852 (2022).
29. Katz, Z.B. *et al.* Mapping translation 'hot-spots' in live cells by tracking single molecules of mRNA and ribosomes. *Elife* **5** (2016).
30. Junod, S.L. *et al.* Dynamics of nuclear export of pre-ribosomal subunits revealed by high-speed single-molecule microscopy in live cells. *iScience* **26**, 107445 (2023).
31. Halstead, J.M. *et al.* Translation. An RNA biosensor for imaging the first round of translation from single cells to living animals. *Science* **347**, 1367–1671 (2015).
32. Ruijtenberg, S., Hoek, T.A., Yan, X. & Tanenbaum, M.E. Imaging Translation Dynamics of Single mRNA Molecules in Live Cells. *Methods Mol Biol* **1649**, 385–404 (2018).
33. Schneider-Poetsch, T. *et al.* Inhibition of eukaryotic translation elongation by cycloheximide and lactimidomycin. *Nat Chem Biol* **6**, 209–217 (2010).
34. Guo, H., Ingolia, N.T., Weissman, J.S. & Bartel, D.P. Mammalian microRNAs predominantly act to decrease target mRNA levels. *Nature* **466**, 835–840 (2010).
35. Sharma, P., Wu, J., Nilges, B.S. & Leidel, S.A. Humans and other commonly used model organisms are resistant to cycloheximide-mediated biases in ribosome profiling experiments. *Nat Commun* **12**, 5094 (2021).

36. Park, Y. *et al.* Versatile Synthetic Route to Cycloheximide and Analogues That Potently Inhibit Translation Elongation. *Angew Chem Int Ed Engl* **58**, 5387–5391 (2019).
37. Abou-Zeid, A.Z., Abd El Hamid, M.M. & El-Sherbini, S.H. Biogenesis and production of cycloheximide by Streptomyces species. *Zentralbl Bakteriol Parasitenkd Infektionskr Hyg* **131**, 419–487 (1976).
38. Paoletti, F. *et al.* Novel fluorescent cycloheximide derivatives for the imaging of protein synthesis. *Biochem Biophys Res Commun* **396**, 258–264 (2010).
39. Roizen, J.L., Zalatan, D.N. & Du Bois, J. Selective intermolecular amination of C-H bonds at tertiary carbon centers. *Angew Chem Int Ed Engl* **52**, 11343–11346 (2013).
40. Koga, Y. *et al.* Discovery of C13-Aminobenzoyl Cycloheximide Derivatives that Potently Inhibit Translation Elongation. *J Am Chem Soc* **143**, 13473–13477 (2021).
41. Chyan, W. & Raines, R.T. Enzyme-Activated Fluorogenic Probes for Live-Cell and in Vivo Imaging. *ACS Chem Biol* **13**, 1810–1823 (2018).
42. Jradi, F.M. & Lavis, L.D. Chemistry of Photosensitive Fluorophores for Single-Molecule Localization Microscopy. *ACS Chem Biol* **14**, 1077–1090 (2019).
43. Wang, L., Frei, M.S., Salim, A. & Johnsson, K. Small-Molecule Fluorescent Probes for Live-Cell Super-Resolution Microscopy. *J Am Chem Soc* **141**, 2770–2781 (2019).
44. Pals, M.J. & Velema, W.A. A Quenched Size-Expanded Nucleotide Reports Activity of the Leukemia Biomarker Terminal Deoxynucleotidyl Transferase (TdT). *Angew Chem Int Ed Engl* **62**, e202302796 (2023).
45. Dziuba, D., Pohl, R. & Hocek, M. Polymerase synthesis of DNA labelled with benzylidene cyanoacetamide-based fluorescent molecular rotors: fluorescent light-up probes for DNA-binding proteins. *Chem Commun (Camb)* **51**, 4880–4882 (2015).
46. Yu, W.T., Wu, T.W., Huang, C.L., Chen, I.C. & Tan, K.T. Protein sensing in living cells by molecular rotor-based fluorescence-switchable chemical probes. *Chem Sci* **7**, 301–307 (2016).
47. Wilson, D.L. & Kool, E.T. Ultrafast Oxime Formation Enables Efficient Fluorescence Light-up Measurement of DNA Base Excision. *J Am Chem Soc* **141**, 19379–19388 (2019).
48. Mondal, I.C. *et al.* Julolidine-based small molecular probes for fluorescence imaging of RNA in live cells. *Org Biomol Chem* **21**, 7831–7840 (2023).
49. Zuo, F. *et al.* Imaging the dynamics of messenger RNA with a bright and stable green fluorescent RNA. *Nat Chem Biol* **20**, 1272–1281 (2024).
50. Paez-Perez, M. & Kuimova, M.K. Molecular Rotors: Fluorescent Sensors for Microviscosity and Conformation of Biomolecules. *Angew Chem Int Ed Engl* **63**, e202311233 (2024).
51. Liu, J., Xu, Y., Stoleru, D. & Salic, A. Imaging protein synthesis in cells and tissues with an alkyne analog of puromycin. *Proc Natl Acad Sci U S A* **109**, 413–418 (2012).
52. Zubradt, M. *et al.* DMS-MaPseq for genome-wide or targeted RNA structure probing in vivo. *Nat Methods* **14**, 75–82 (2017).
53. Myasnikov, A.G. *et al.* Structure-function insights reveal the human ribosome as a cancer target for antibiotics. *Nat Commun* **7**, 12856 (2016).
54. Garreau de Loubresse, N. *et al.* Structural basis for the inhibition of the eukaryotic ribosome. *Nature* **513**, 517–522 (2014).
55. Dorner, K., Ruggeri, C., Zemp, I. & Kutay, U. Ribosome biogenesis factors-from names to functions. *EMBO J* **42**, e112699 (2023).
56. Lavdovskaia, E. *et al.* A roadmap for ribosome assembly in human mitochondria. *Nat Struct Mol Biol* **31**, 1898–1908 (2024).

57. Jagannathan, S., Reid, D.W., Cox, A.H. & Nicchitta, C.V. De novo translation initiation on membrane-bound ribosomes as a mechanism for localization of cytosolic protein mRNAs to the endoplasmic reticulum. *RNA* **20**, 1489–1498 (2014).
58. Ruthardt, N., Lamb, D.C. & Brauchle, C. Single-particle tracking as a quantitative microscopy-based approach to unravel cell entry mechanisms of viruses and pharmaceutical nanoparticles. *Mol Ther* **19**, 1199–1211 (2011).
59. Wang, C., Han, B., Zhou, R. & Zhuang, X. Real-Time Imaging of Translation on Single mRNA Transcripts in Live Cells. *Cell* **165**, 990–1001 (2016).
60. Renner, M., Wang, L., Levi, S., Hennekinne, L. & Triller, A. A Simple and Powerful Analysis of Lateral Subdiffusion Using Single Particle Tracking. *Biophys J* **113**, 2452–2463 (2017).
61. Stephens, S.B. & Nicchitta, C.V. Divergent regulation of protein synthesis in the cytosol and endoplasmic reticulum compartments of mammalian cells. *Mol Biol Cell* **19**, 623–632 (2008).
62. Yan, X., Hoek, T.A., Vale, R.D. & Tanenbaum, M.E. Dynamics of Translation of Single mRNA Molecules In Vivo. *Cell* **165**, 976–989 (2016).
63. Carter, S.D. *et al.* Ribosome-associated vesicles: A dynamic subcompartment of the endoplasmic reticulum in secretory cells. *Sci Adv* **6**, eaay9572 (2020).
64. Waisman, A. *et al.* Cell cycle dynamics of mouse embryonic stem cells in the ground state and during transition to formative pluripotency. *Sci Rep* **9**, 8051 (2019).
65. Lin, L., Zou, Y. & Zhang, D. Silencing ribosome biogenesis regulator 1 homolog (RRS1) inhibits angiogenesis and cisplatin resistance of lung cancer cells by activating ferroptosis mediated by p53 pathway. *Tissue Cell* **94**, 102796 (2025).
66. Pan, H. *et al.* RBIS regulates ribosome biogenesis to affect progression in lung adenocarcinoma. *J Transl Med* **22**, 1147 (2024).
67. Fan, H. & Penman, S. Regulation of protein synthesis in mammalian cells. II. Inhibition of protein synthesis at the level of initiation during mitosis. *J Mol Biol* **50**, 655–670 (1970).
68. Xu, C.S.P., S.; Hayworth, K. J.; Hess, H. F. (ed. J.R.C. OpenOrganelle) (2020).
69. Fraser, H.B., Hirsh, A.E., Giaever, G., Kumm, J. & Eisen, M.B. Noise minimization in eukaryotic gene expression. *PLoS Biol* **2**, e137 (2004).
70. Tahmasebi, S., Amiri, M. & Sonenberg, N. Translational Control in Stem Cells. *Front Genet* **9**, 709 (2018).
71. Breznak, S.M., Kotb, N.M. & Rangan, P. Dynamic regulation of ribosome levels and translation during development. *Semin Cell Dev Biol* **136**, 27–37 (2023).
72. Wang, R. & Amoyel, M. mRNA Translation Is Dynamically Regulated to Instruct Stem Cell Fate. *Front Mol Biosci* **9**, 863885 (2022).
73. Atlasi, Y. *et al.* The translational landscape of ground state pluripotency. *Nat Commun* **11**, 1617 (2020).
74. Loebel, D.A., Watson, C.M., De Young, R.A. & Tam, P.P. Lineage choice and differentiation in mouse embryos and embryonic stem cells. *Dev Biol* **264**, 1–14 (2003).
75. Martin, G.R. Isolation of a pluripotent cell line from early mouse embryos cultured in medium conditioned by teratocarcinoma stem cells. *Proc Natl Acad Sci U S A* **78**, 7634–7638 (1981).
76. Semrau, S. *et al.* Dynamics of lineage commitment revealed by single-cell transcriptomics of differentiating embryonic stem cells. *Nat Commun* **8**, 1096 (2017).
77. Garcia-Blay, O. *et al.* Multimodal screen identifies noise-regulatory proteins. *Dev Cell* **60**, 133–151 e112 (2025).

78. Li, D. & Wang, J. Ribosome heterogeneity in stem cells and development. *J Cell Biol* **219** (2020).
79. Holt, C.E., Martin, K.C. & Schuman, E.M. Local translation in neurons: visualization and function. *Nat Struct Mol Biol* **26**, 557–566 (2019).
80. You, K.T., Park, J. & Kim, V.N. Role of the small subunit processome in the maintenance of pluripotent stem cells. *Genes Dev* **29**, 2004–2009 (2015).
81. Saba, J.A., Liakath-Ali, K., Green, R. & Watt, F.M. Translational control of stem cell function. *Nat Rev Mol Cell Biol* **22**, 671–690 (2021).
82. Sampath, P. *et al.* A hierarchical network controls protein translation during murine embryonic stem cell self-renewal and differentiation. *Cell Stem Cell* **2**, 448–460 (2008).
83. Ingolia, N.T., Lareau, L.F. & Weissman, J.S. Ribosome profiling of mouse embryonic stem cells reveals the complexity and dynamics of mammalian proteomes. *Cell* **147**, 789–802 (2011).
84. Blair, J.D., Hockemeyer, D., Doudna, J.A., Bateup, H.S. & Floor, S.N. Widespread Translational Remodeling during Human Neuronal Differentiation. *Cell Rep* **21**, 2005–2016 (2017).
85. Baser, A. *et al.* Onset of differentiation is post-transcriptionally controlled in adult neural stem cells. *Nature* **566**, 100–104 (2019).
86. Corsini, N.S. *et al.* Coordinated Control of mRNA and rRNA Processing Controls Embryonic Stem Cell Pluripotency and Differentiation. *Cell Stem Cell* **22**, 543–558 e512 (2018).
87. Pauklin, S. & Vallier, L. The cell-cycle state of stem cells determines cell fate propensity. *Cell* **155**, 135–147 (2013).
88. Koledova, Z. *et al.* Cdk2 inhibition prolongs G1 phase progression in mouse embryonic stem cells. *Stem Cells Dev* **19**, 181–194 (2010).
89. Martínková, S. *et al.* Ribosome transfer via tunnelling nanotubes rescues protein synthesis in pancreatic cancer cells. *bioRxiv*, 2024.2006.2006.597772 (2025).
90. Gatie, M.I., Assabgui, A.R. & Kelly, G.M. The Zen of XEN: insight into differentiation, metabolism and genomic integrity. *Cell Death & Disease* **9**, 1075 (2018).
91. Shimosato, D., Shiki, M. & Niwa, H. Extra-embryonic endoderm cells derived from ES cells induced by GATA Factors acquire the character of XEN cells. *BMC Developmental Biology* **7**, 80 (2007).
92. Besse, F. & Ephrussi, A. Translational control of localized mRNAs: restricting protein synthesis in space and time. *Nature Reviews Molecular Cell Biology* **9**, 971–980 (2008).
93. Steward, O. & Schuman, E.M. Protein synthesis at synaptic sites on dendrites. *Annu Rev Neurosci* **24**, 299–325 (2001).
94. Parekkadan, B. *et al.* Cell-cell interaction modulates neuroectodermal specification of embryonic stem cells. *Neurosci Lett* **438**, 190–195 (2008).
95. Hardin, J. & Armstrong, N. Short-range cell-cell signals control ectodermal patterning in the oral region of the sea urchin embryo. *Dev Biol* **182**, 134–149 (1997).
96. Denes, L.T., Kelley, C.P. & Wang, E.T. Microtubule-based transport is essential to distribute RNA and nascent protein in skeletal muscle. *Nature Communications* **12**, 6079 (2021).
97. Simpson, L.J., Tzima, E. & Reader, J.S. Mechanical Forces and Their Effect on the Ribosome and Protein Translation Machinery. *Cells* **9**, 650 (2020).
98. Ni, C. & Buszczak, M. The homeostatic regulation of ribosome biogenesis. *Semin Cell Dev Biol* **136**, 13–26 (2023).
99. Ni, C. *et al.* A programmed decline in ribosome levels governs human early neurodevelopment. *Nat Cell Biol* **27**, 1240–1255 (2025).

100. Rangaraju, V., Lauterbach, M. & Schuman, E.M. Spatially Stable Mitochondrial Compartments Fuel Local Translation during Plasticity. *Cell* **176**, 73–84.e15 (2019).
101. Genuth, N.R. *et al.* A stem cell roadmap of ribosome heterogeneity reveals a function for RPL10A in mesoderm production. *Nat Commun* **13**, 5491 (2022).
102. McHedlov-Petrossyan, N.O., Cheipesh, T.A., Roshal, A.D., Doroshenko, A.O. & Vodolazkaya, N.A. Fluorescence of aminofluoresceins as an indicative process allowing one to distinguish between micelles of cationic surfactants and micelle-like aggregates. *Methods Appl Fluoresc* **4**, 034002 (2016).
103. van Mierlo, G. *et al.* Integrative Proteomic Profiling Reveals PRC2-Dependent Epigenetic Crosstalk Maintains Ground-State Pluripotency. *Cell Stem Cell* **24**, 123–137 e128 (2019).
104. Desai, R.V. *et al.* A DNA repair pathway can regulate transcriptional noise to promote cell fate transitions. *Science* **373**, eabc6506 (2021).
105. Incarnato, D., Morandi, E., Simon, L.M. & Oliviero, S. RNA Framework: an all-in-one toolkit for the analysis of RNA structures and post-transcriptional modifications. *Nucleic Acids Res* **46**, e97 (2018).
106. Schindelin, J. *et al.* Fiji: an open-source platform for biological-image analysis. *Nat Methods* **9**, 676–682 (2012).
107. Ershov, D. *et al.* TrackMate 7: integrating state-of-the-art segmentation algorithms into tracking pipelines. *Nat Methods* **19**, 829–832 (2022).
108. Virtanen, P. *et al.* SciPy 1.0: fundamental algorithms for scientific computing in Python. *Nat Methods* **17**, 261–272 (2020).
109. Rossum, G.V. & Drake, F.L. *Python 3 Reference Manual*. (CreateSpace, 2009).
110. Bisong, E. *Building Machine Learning and Deep Learning Models on Google Cloud Platform*. (Apress, Berkeley, CA; 2019).
111. Waskom, M.L. seaborn: statistical data visualization. *Journal of Open Source Software* **6**, 3021 (2021).

ACKNOWLEDGEMENTS
We thank Dr. Hendrik Marks (Radboud University) for the mESC-E14 cells; Prof. Leor Weinberger (University of Miami) for the NANOG-GFP mESC-E14 cells; Prof. Ger Pruijn (Radboud University) for providing SH-SY5Y cells, Dr. Klaas Mulder (Radboud University) for providing HCT 116 and U2OS cells, Prof. Wilhelm Huck (Radboud University) for providing HeLa cells and Dr. Wenny Peeters (Radiotherapy & OncoImmunology Laboratory, Department of Radiation Oncology, Radboudumc) for providing MCF 10A cells. This work has received funding from the European Research Council under the European Union's Horizon Europe research and innovation programme under grant agreement number 101041939 (ChOICE) to M.M.K.H and 101041938 (RIBOCHEM) to W.A.V. M.M.K.H. further acknowledges generous support from the Christine Mohrmann fellowship and the Oncode Institute, which is partly financed by the Dutch Cancer Society.

AUTHOR CONTRIBUTIONS
Conceptualization: WAV, MMKH
Methodology: GP, CG, XH, WAV, MMKH
Investigation: GP, CG, XH, PY
Visualization: GP, CG, XH
Funding acquisition: WAV, MMKH
Project administration: GP, CG, XH, WAV, MMKH
Supervision: WAV, MMKH
Writing – original draft: GP, CG, XH, WAV, MMKH
Writing – review & editing: GP, CG, XH, PY, WAV, MMKH

COMPETING INTERESTS STATEMENT
A patent related to this work has been filed with:
Applicant: STICHTING RADBOUD UNIVERSITEIT
Inventors: Maike Hansen, Willem Velema
Application Number: NL2025/150006
Status of the application: PCT application filed
Specific aspects of the manuscript covered in the patent application: Probe for single cell ribosome imaging and tracking; RiboBright probe
Application claims priority from: NL 2039232 (NL application)

All other authors declare no competing interests.

FIGURE LEGENDS

Figure 1. RiboBright fluoresces with restricted rotation.

a, Structure of cycloheximide and proposed structure of fluorescent probes with modifications at the C13 position of cycloheximide. **b,** Interactions of cycloheximide with the E-site of the ribosome. (PDB: 5LKS).[53] **c,** Schematic concept of using fluorescent rotor probes to visualize ribosomes with fluorescence microscopy. **d,** Probes **1**-**3** were synthesized starting from CHX, employing a previously published procedure for C13 modification and amide coupling to CCVJ fluorophores with varied linker length. **e,** *In vitro* activity of probes **1**-**3** and CHX. Average and standard deviation of triplicate measurements (n=3 technical replicates). **f,** Uncorrected fluorescent emission spectra (λ_{ex}=460 nm) of probes **1**-**3**, in 1/4 PBS/Glycerol and PBS only (inset). **g,** Representative single z-plane images of HEK293T/17 cells incubated with 10 μM probes **1**-**3** (repeated twice with similar results). The insets for probe **2** and **3**, display the same image with enhanced contrast. Images were acquired with 100x/1.40 NA oil objective. Scale bars are 15 μm and 5 μm (inset). **h,** Fluorescent intensity profile of the indicated cross sections in panel **g**. **i,** Different z-positions of HEK293T/17 cells stained with 10 μM of probe **1** – RiboBright (repeated twice with similar results). Scale bars are 10 μm.

Figure 2. **Cellular performance of RiboBright.**

a, Cellular translation inhibition by RiboBright and CHX assessed by an OPP assay. **b,** Scatter plot showing DMS induced mutation rate of ribosomal nucleotides in RiboBright or CHX treated and DMSO treated samples. **c,** Left: Representative single z-plane images of HEK293T/17 cells incubated with 10 μM RiboBright only and pretreated with 100 μM cycloheximide (top) or phyllantoside (bottom) for 30 min. The insets for CHX and phyllantoside display the same image with enhanced contrast. Right: Fluorescent intensity profile of indicated cross sections is shown. Images were acquired with 100x/1.40 NA oil objective (repeated twice with similar results). Scale bars are 15 μm. **d,** Left: Representative single z-plane images of HEK293T/17 cells incubated with 10 μM RiboBright together with ER (top) and mitochondria (bottom) specific counterstains. Images were acquired with 100x/1.40 NA oil objective. Scale bars are 15 μm. Right: Quantification of colocalization between RiboBright and organelle-specific markers in 3D using Manders' coefficients (M1 and M2). Violin plots show the data distribution; inner boxes mark the IQR (25th–75th percentiles) and white dots indicate medians. M1 (top) represents the fraction of RiboBright signal overlapping with ER or mitochondria; M2 (bottom) represents the fraction of ER or mitochondria signal overlapping with RiboBright. Each dot corresponds to a single image field, colored by biological replicate (n=2 biological replicates; 61 fields total). Group differences were tested with a two-sided Mann–Whitney U test comparing ER and mitochondria conditions. Exact p-value and median fold changes in M1 (RiboBright–ER vs. RiboBright–mitochondria): p = 2.07e-11, FC = 2.12; M2 (RiboBright–ER vs. RiboBright–mitochondria): p = 4.59e-05, FC = 0.98. Significance levels: ns, $p > 0.05$; *$p < 0.05$; **$p < 0.01$; ***$p < 0.001$.

Figure 3. RiboBright allows tracking of ribosome movement in single cells.

a, Representative image of HEK293T/17 cells (from two biological replicates) stained with 10 μM RiboBright (left) and corresponding trajectories obtained by tracking individual foci (right). Single z-plane images were acquired with 100x/1.40 NA oil objective. Scale bars are 15 μm. **b,** Example trajectories (from two biological replicates) displaying apparent super (pink), normal (light blue), and confined (dark blue) movement. Images were acquired with 100x/1.40 NA oil objective. Scale bars are 1 μm. **c,** MSD curves of the trajectories shown in panel **b**, and their associated α values.

d, Example trajectory (from two biological replicates) showing transitioning between super (pink) and normal (light blue) diffusion (upper panel). Single z-plane images were acquired with 100x/1.40 NA oil objective. Scale bars are 1 μm. The Pc values increase as the area of confinement decreases, while the instantaneous diffusion coefficient (D_i) decreases during Brownian-defined periods (lower panel). **e,** Averaged MSD curves of the trajectories of two biological replicates (dashed and solid line), classified into super (pink), normal (light blue), and confined (dark blue) movement based on their α values. **f,** Average diffusion coefficient of all tracked trajectories for two replicates (n=2). Inset: Diffusion coefficient of all tracked trajectories. The box plot shows the median and the interquartile range, and the whiskers represent the dispersion of the data. Each dot represents one datapoint from two replicates. **g,** Average diffusion coefficient of single cells. The inset shows examples of cellular segmentation. Box plots display the median and interquartile range; whiskers represent data dispersion, and error bars show the standard deviation. Each dot corresponds to a single datapoint from two biological replicates. Number of cells analyzed per type of diffusion: rep1 — confined: 203, normal: 190, super: 163; rep2 — confined: 192, normal: 180, super: 151.

Figure 4. RiboBright enables ribosome quantification across diverse contexts and reveals mESCs to have the lowest per-ribosome translational efficiency.
a, Representative single z-plane images of mESCs, HCT 116, HEK293T/17, MCF 10A, SH-SY5Y, PC-9, HeLa, U2OS, SK-MEL-28, and PANC-1 cells stained with 10 μM RiboBright. Images were acquired with 100x/1.40 NA oil objective (n=2 biological replicates). Scale bars are 15 μm, 1 μm. **b,** Distributions of flow cytometry data show live mESCs, HCT 116, HEK293T/17, MCF 10A, SH-SY5Y, PC-9, HeLa, U2OS, SK-MEL-28, and PANC-1 cells stained with 10 μM RiboBright. The unstained control is subtracted for reach cell type. **c,** Representative single z-plane images of fixed HEK293T/17 cells co-stained with OPP and RiboBright. Images were acquired with 100x/1.40 NA oil objective (n=2 biological replicates). Scale bars are 10 μm. **d,** Scatter plot showing the relationship between OPP intensity (i.e., translation levels) and RiboBright intensity (i.e., ribosome content) measured in single cells in mESCs (400 cells), HCT 116 (557 cells), HEK293T/17 (618 cells), MCF 10A (657 cells), SH-SY5Y (402 cells), PC-9 (284 cells), HeLa (498 cells), U2OS (502 cells), SK-MEL-28 (339 cells) and PANC-1 (712 cells) cells within one biological replicate. Each data point corresponds to an individual cell per cell type. **e,** Pearson correlation between the RiboBright intensities and variability (measured as Fano factor = σ^2/μ) across the cell lines shown in panel **d and Supplementary Fig. 3a**. **f,** Average per-ribosome translational efficiency measured as the ratio between OPP and RiboBright intensity (= OPP (new protein synthesis)/RiboBright (Ribosome content)) measured across the cell lines shown in panel **d and Supplementary Fig. 3a**. **e-f,** Data was acquired for 888 mES cells, 2132 HCT 116 cells, 1338 HEK293T/17 cells, 1412 MCF 10A cells, 755 SH-SY5Y cells, 730 PC-9 cells, 1165 HeLa cells, 1041 U2OS cells, 941c SK-MEL-28 cells and 1675 PANC-1 cells, each dot indicates the mean of the two biological replicates (n=2).

Figure 5. RiboBright uncovers lineage-specific ribosome behavior in differentiating mESCs.
a, Schematic showing that upon exposure to RA, mESCs can differentiate either into ectoderm-like cells (ECT, CD24+) or extraembryonic endoderm-like (XEN, CD140a+) cells. **b,** Flow cytometry analysis of cells co-stained with CD24, CD140, and RiboBright 72 hours after differentiation induction in the presence of RA (right) or maintained in LIF-containing control conditions (left). Data represent combined results from two independent differentiation

experiments, each with three technical replicates. **c,** Representative scatter plot (left) shows the distribution of CD24+CD140a-, CD24+CD140a+, and CD24-CD140a+, and CD24-CD140a- cell populations after 72 hours of RA-induced differentiation. Kernel density estimates display the normalized RiboBright intensity for CD24+CD140a-, CD24+CD140a+, and CD24-CD140a+ populations, overlaid with the distribution of the CD24-CD140a- population as a reference. The inset bar chart summarizes the mean ± SD of normalized RiboBright intensity for each population, with individual data points representing technical replicate means. Statistical significance between populations was assessed using a two-sided, paired t-test across technical replicates (n= 3 technical replicates, >7000 cells per replicate) within biological replicates (n= 2): Q1 vs. Q4, p = 4.77e-06; Q2 vs. Q4, p = 1.45e-04; Q3 vs. Q4, p = 8.41e-08. **d,** Representative single z-plane images of CD24, CD140a and RiboBright stained cells 72 hours after inducing differentiation in the presence of RA (n=3 technical replicates). Images were acquired with 60x/1.42 NA oil objective. Scale bars are 40 μm, 10 μm. **e,** Distribution of average RiboBright intensity at the single-cell level across four cell populations: CD24-/CD140a-, CD24+, CD140a+ and CD24+/CD140a+. Data represent 242 CD24+ cells, 280 CD140a+ cells, 303 CD24-/CD140a- cells, and 0 CD24+/CD140a+ cells, from one differentiation experiment (n=3 technical replicates). Each dot corresponds to an individual cell; inner box = IQR (25th–75th percentiles) with white dot = median; minima/maxima are limited to the most extreme points within this range. Statistical comparisons between cell populations were performed using the two-sided Mann–Whitney U test. Significant differences are indicated exact p value on the plots. Exact p-value and mean fold changes (RiboBright intensity of group2 relative to group1) are as follows: CD24-/CD140a- vs CD24+: p = 3.94e-05, FC = 1.07; CD24+ vs CD140a+: p = 0.06, FC = 0.96; CD24-/CD140a- vs CD140a+: p = 7.71e-06, FC = 0.90 (for the corresponding comparisons). **f,** Single-cell area distribution of CD24-/CD140a-, CD24+, and CD140a+ cells 72 hours after induction of differentiation. Data represent 303 CD24-/CD140a- cells, 242 CD24+ cells, 280 CD140a+ cells, and 0 CD24+/CD140a+ cells, from one differentiation experiment (n=3 technical replicates). Each dot represents an individual cell; inner box = IQR (25th–75th percentiles) with white dot = median; minima/maxima are limited to the most extreme points within this range. Statistical comparisons between cell populations were performed using the two-sided Mann–Whitney U test. Exact p-value and mean fold changes are as follows: CD24-/CD140a- vs CD24+: p = 6.65e-04, FC = 0.83; CD24+ vs CD140a+: p = 2.64e-26, FC = 1.68; CD24-/CD140a- vs CD140a+: p = 1.17e-28, FC = 1.39 (for the corresponding comparisons). **g,** Average diffusion coefficient of each type of diffusion measured in CD24-/CD140a-, CD24+ and CD140a+ cells 72 hours after differentiation induction. Each dot represents a single technical replicate (n=3 per biological replicate) and each shape represents a biological replicate (n = 3). Error bars represent the standard deviation across all technical and biological replicates. Exact p-value and fold change of mean in Confined cell types: CD24-CD140a-/CD24+: p = 2.91e-02, FC = 0.90; CD24-CD140a-/CD140a+: p = 5.76e-03, FC = 1.16; CD24+/ CD140a+: p = 2.54e-05, FC = 1.29; Normal cell types: CD24-CD140a-/CD24+: p = 6.71 e-03, FC = 0.90; CD24-CD140a-/CD140a+: p = 7.66e-05, FC = 1.22; CD24+/ CD140a+: p = 2.00e-07, FC = 1.35; Super cell types: CD24-CD140a-/CD24+: p = 4.29e-02, FC= 0.90; CD24-CD140a-/CD140a+: p = 4.23e-04, FC = 1.29; CD24+/ CD140a+: p = 1.14e-05, FC =1.42. Statistical comparisons between cell populations were performed using the two-sided Mann–Whitney U test. Significance: ns, $p > 0.05$; *$p < 0.05$; **$p < 0.01$; ***$p < 0.001$.

Figure 6. RiboBright reveals prominent translational hubs specific to the ectoderm-like lineage at the onset of differentiation.

a, Representative single z-plane images of mESCs stained with OPP (grey) and RiboBright (cyan) during 0, 24, 48 and 72 hours of differentiation. In LIF (undifferentiated) and RA (differentiating) culture conditions (n=3 technical replicates). Images were acquired with 60x/1.42 NA oil objective. Scale bars are 40 μm and 10 μm (right). **b**, Representative single z-plane image of translational hubs where both RiboBright and OPP signal colocalizes (left) (n=3 technical replicates). Images were acquired with 60x/1.42 NA oil objective. Scale bar is 10 μm. Fluorescent intensity profile of the indicated cross sections in the left images (right). **c,** Percentage of CD24-CD140a-, CD24+ and CD140a+ cells from Figure 5d that contain bright RiboBright hubs (RiboBright pixel intensity is higher than 4000). **d,** Average changes in the percentages of CD24+, CD140a+, and CD24-CD140a- cell populations at 0, 24, 48, and 72 hours during differentiation, calculated relative to the 0-hour baseline. Shaded areas indicate the standard deviation derived from three biological replicates, each consisting of two technical replicates. Statistical significance at 72 hours was assessed using t-test (unpaired, two-tailed) relative to the 0-hour baseline: CD140a-CD24+, p = 1.05e-4; CD140a+CD24+, p = 1.21e-04; CD140a+CD24-, p = 0.02. **e,** Ratio of OPP to RiboBright intensity (corresponding to Supplementary Figure 4d) in LIF (undifferentiated) and RA (differentiated) culture conditions at 0, 24, 48, and 72 hours. Cell counts per condition are as follows: 0 hours – LIF: 314 cells; 24 hours – LIF: 1230 cells, RA: 1404 cells; 48 hours – LIF: 2517 cells, RA: 1409 cells; 72 hours – LIF: 3118 cells, RA: 2643 cells (n=3 technical replicates). Each dot represents a single-cell measurement. Box plots show the median (centre line) and interquartile range (box); whiskers extend to the most extreme data points within 1.5×IQR. Statistical significance between LIF and RA at each time point was determined using the two-sided, non-parametric Mann–Whitney U test: 24h, p = 1.31e-09; 48h, p = 1.41e-88; 72h, p = 2.04e-117. The median fold change (RA / LIF) at 24, 48, and 72 hours is 1.02, 1.07, and 1.08, respectively. **f,** Pearson correlation between OPP intensity and RiboBright intensity (shown in panel d) at 72 hours under LIF (undifferentiated, left) and RA (differentiated, right) culture conditions. Each dot represents a single-cell measurement. **g,** Representative single z-plane images showing merged RiboBright (cyan) with ER (red, top) or mitochondria (magenta, bottom) signals under LIF (left) and RA (right) conditions. Scale bar: 15 μm. **h,** Violin plots showing the distribution of Manders' coefficients (M1 or M2) of RiboBright and ER or RiboBright and Mitochondria between LIF and RA conditions. Each dot represents a single data point, colored by biological replicate (n=2); inner box = IQR (25th–75th percentiles) with white dot = median; minima/maxima are limited to the most extreme points within this range. Significance determined with two-sided Mann–Whitney U test for cells cultured in LIF vs. RA conditions. Exact p-vale and median fold change (RA / LIF) for each dataset is as follows: M1: RiboBright vs. ER: p = 0.08, FC = 0.98, M2: RiboBright vs. ER: p = 0.56, FC = 1.00; M1: RiboBright vs. Mito: p = 4.3e-04, FC = 1.43, M2: RiboBright vs. Mito: p = 0.02, FC = 0.97. Significance: ns, $p > 0.05$; *$p < 0.05$; **$p < 0.01$; ***$p < 0.001$.

Editorial Summary:
Ribosomes drive protein synthesis, but their dynamics are hard to visualize. Here, authors introduce RiboBright, a fluorescent probe that illuminates ribosomes in live and fixed cells, revealing cell-type specific content, organization, and movement.
Peer review information: *Nature Communications* thanks Lei Lei who co-reviewed with Yuchen Sun; and the other, anonymous, reviewer(s) for their contribution to the peer review of this work. A peer review file is available.

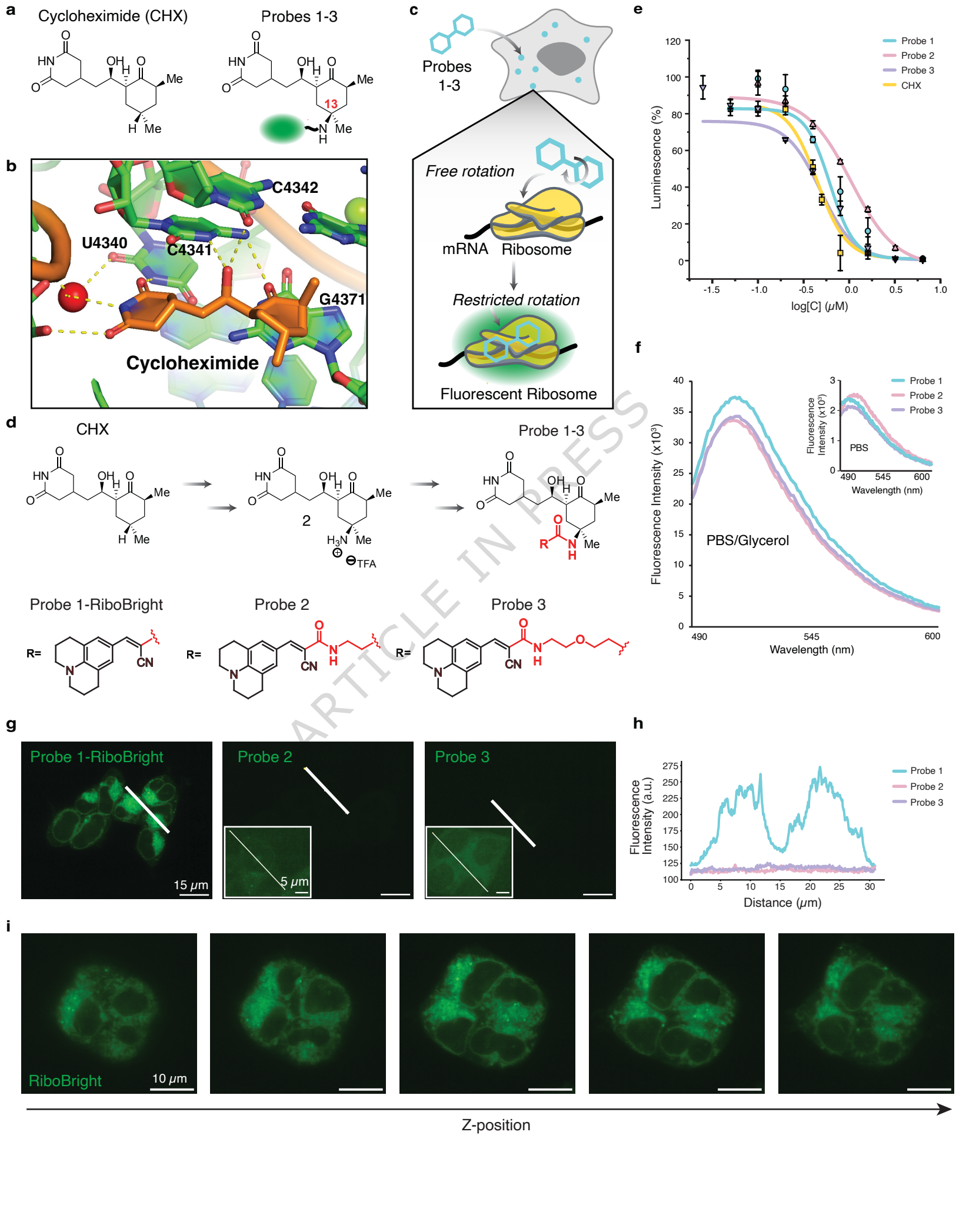

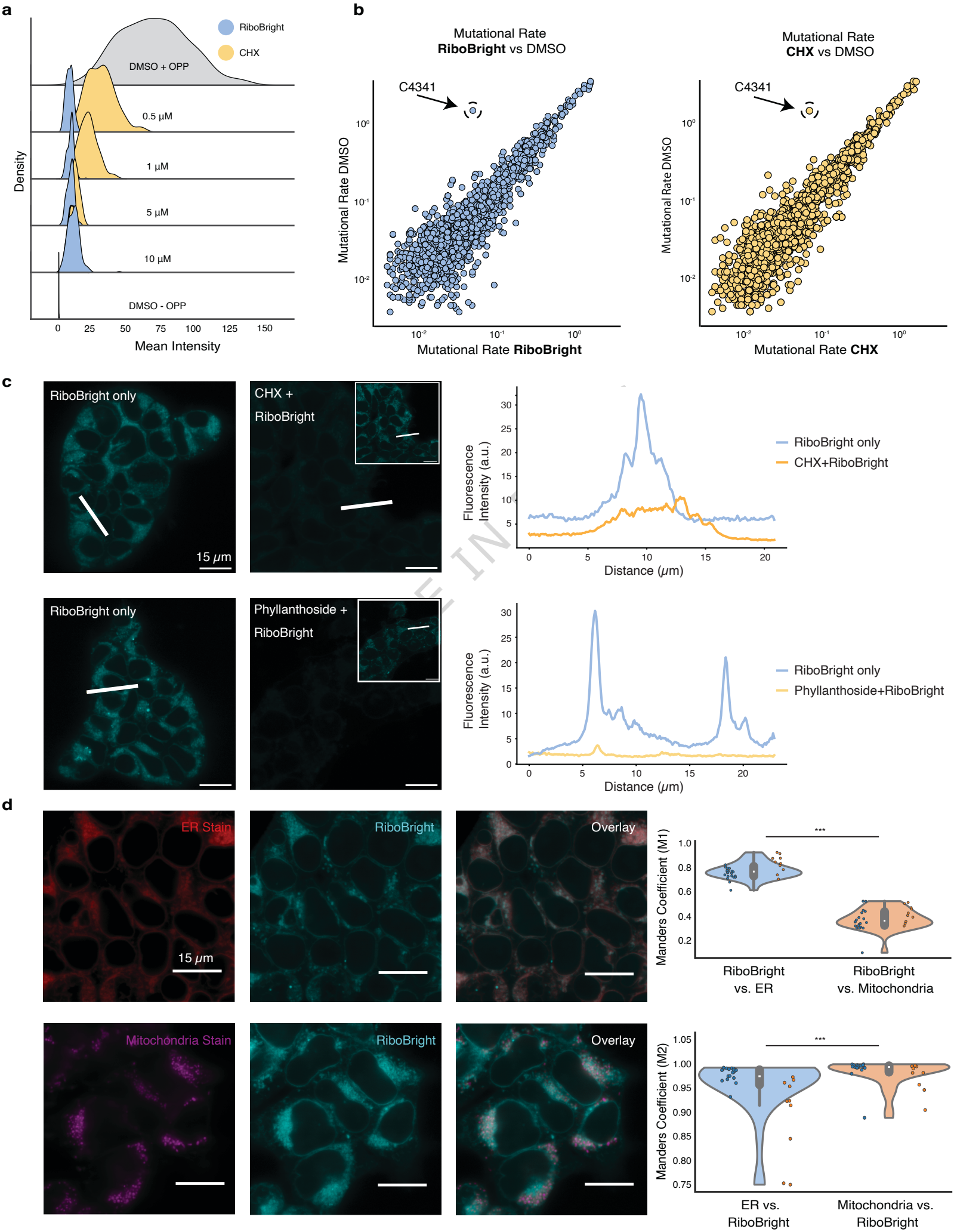
a
RiboBright
CHX
DMSO + OPP
0.5 µM
1 µM
5 µM
10 µM
DMSO - OPP
Density
0
25
50
75
100
125
150
Mean Intensity
b
Mutational Rate
RiboBright vs DMSO
C4341
Mutational Rate DMSO
Mutational Rate RiboBright
Mutational Rate
CHX vs DMSO
C4341
Mutational Rate DMSO
Mutational Rate CHX
c
RiboBright only
15 µm
CHX +
RiboBright
Fluorescence
Intensity (a.u.)
Distance (µm)
RiboBright only
CHX+RiboBright
RiboBright only
Phyllanthoside +
RiboBright
Fluorescence
Intensity (a.u.)
Distance (µm)
RiboBright only
Phyllanthoside+RiboBright
d
ER Stain
15 µm
RiboBright
Overlay
Manders Coefficient (M1)
***
RiboBright
vs. ER
RiboBright
vs. Mitochondria
Mitochondria Stain
RiboBright
Overlay
Manders Coefficient (M2)
***
ER vs.
RiboBright
Mitochondria vs.
RiboBright

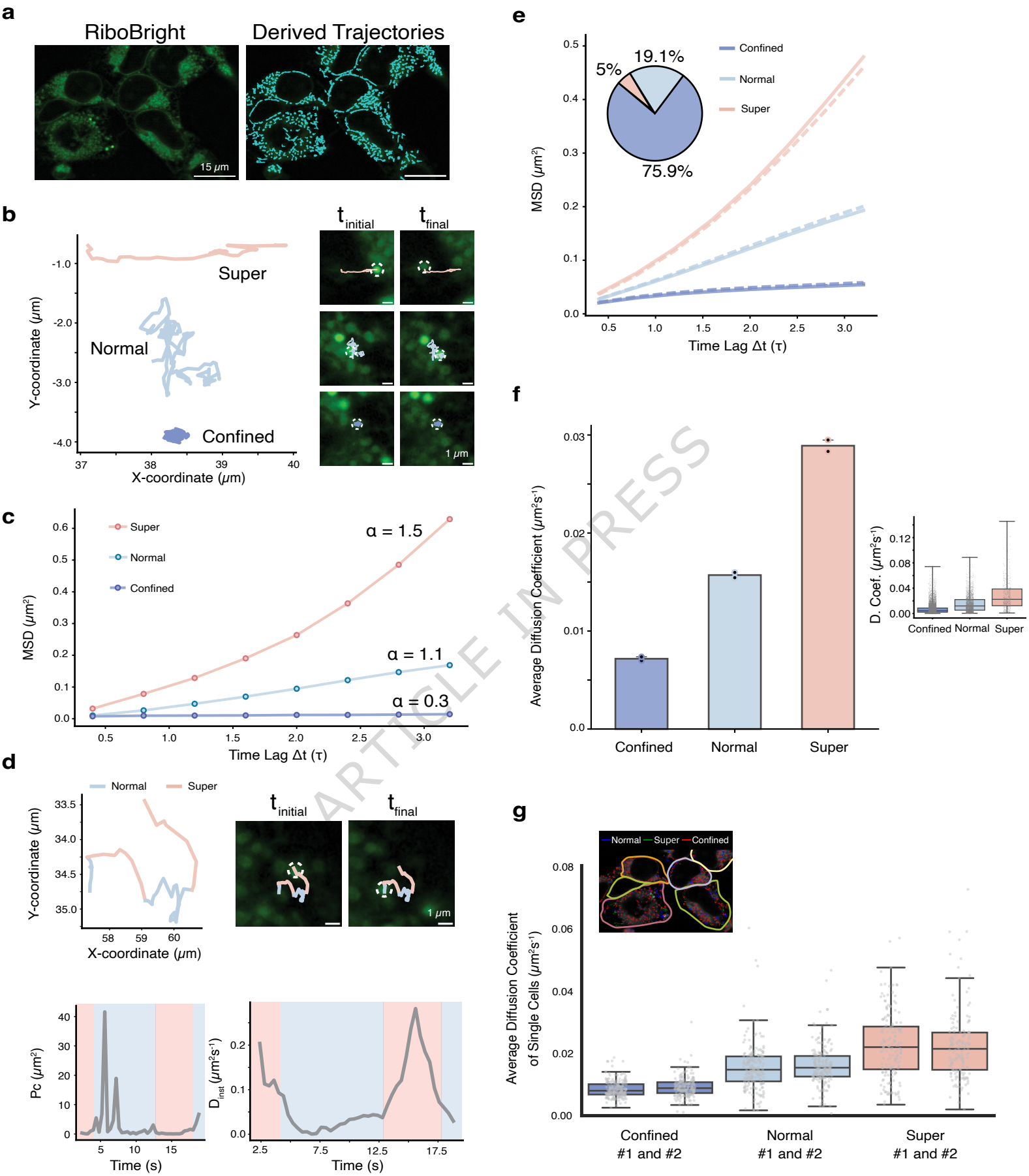

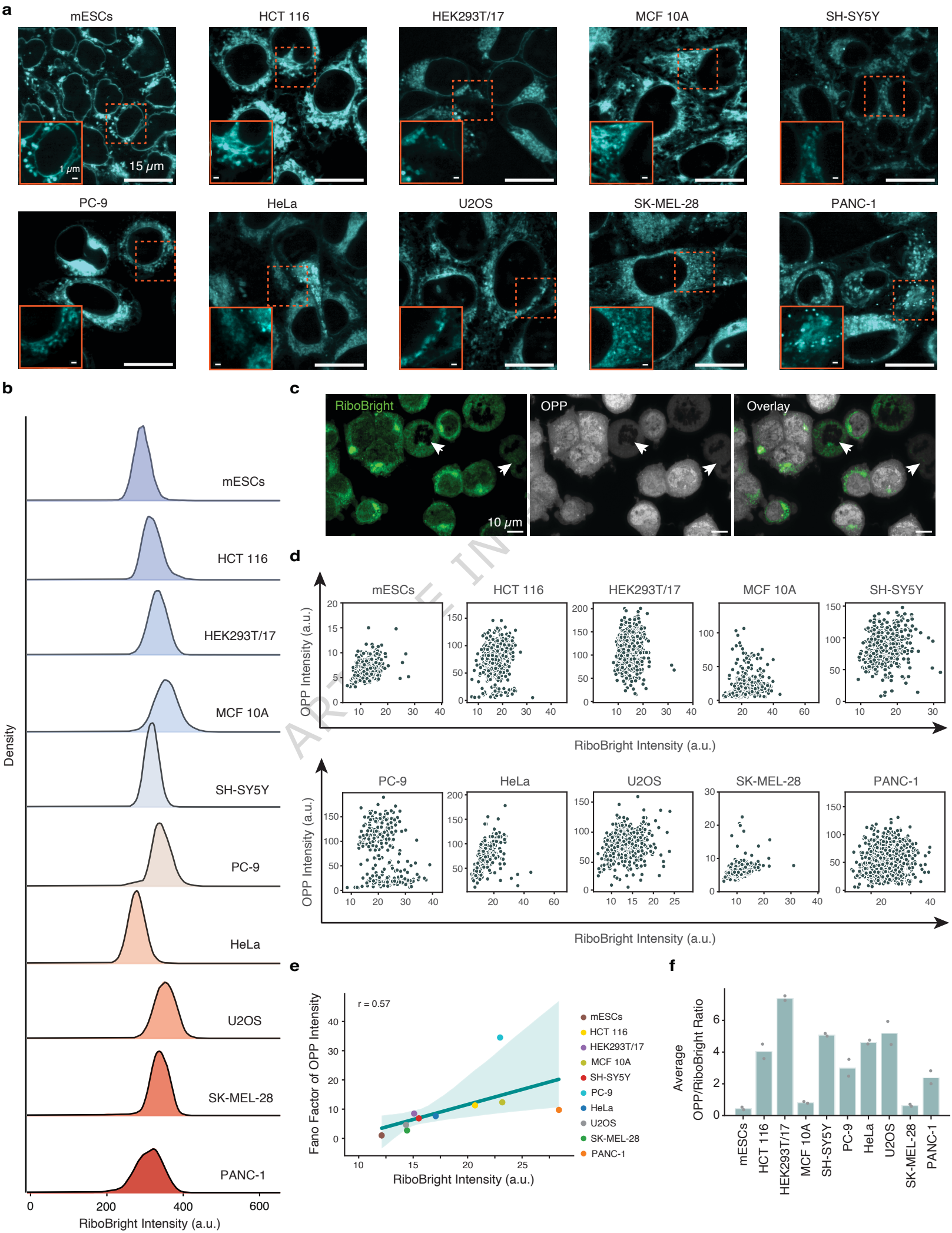
a
mESCs
HCT 116
HEK293T/17
MCF 10A
SH-SY5Y
1 μm
15 μm
PC-9
HeLa
U2OS
SK-MEL-28
PANC-1
b
Density
mESCs
HCT 116
HEK293T/17
MCF 10A
SH-SY5Y
PC-9
HeLa
U2OS
SK-MEL-28
PANC-1
0
200
400
600
RiboBright Intensity (a.u.)
c
RiboBright
OPP
Overlay
10 μm
d
mESCs
HCT 116
HEK293T/17
MCF 10A
SH-SY5Y
PC-9
HeLa
U2OS
SK-MEL-28
PANC-1
OPP Intensity (a.u.)
RiboBright Intensity (a.u.)
e
r = 0.57
Fano Factor of OPP Intensity
RiboBright Intensity (a.u.)
mESCs
HCT 116
HEK293T/17
MCF 10A
SH-SY5Y
PC-9
HeLa
U2OS
SK-MEL-28
PANC-1
f
Average OPP/RiboBright Ratio
mESCs
HCT 116
HEK293T/17
MCF 10A
SH-SY5Y
PC-9
HeLa
U2OS
SK-MEL-28
PANC-1

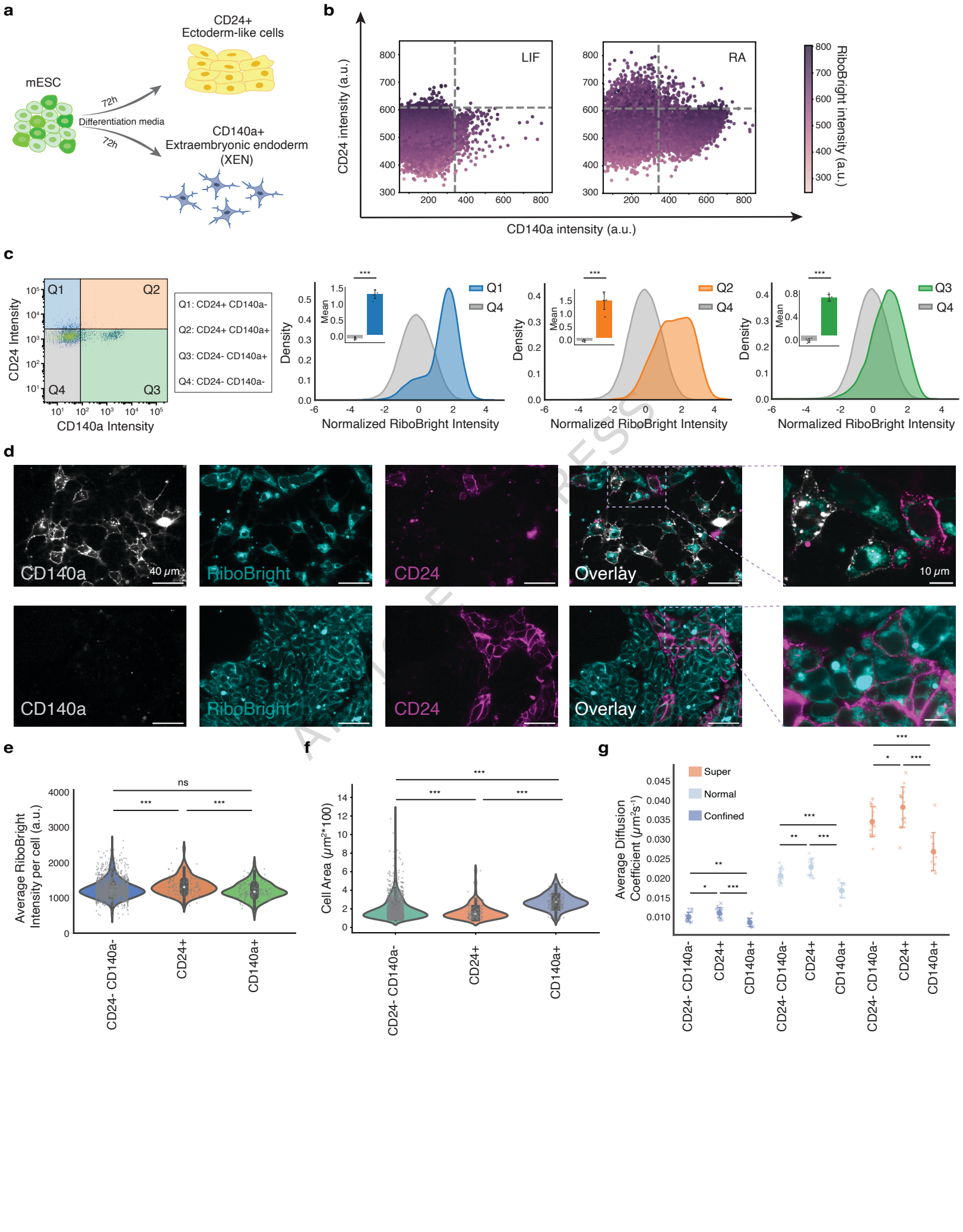
a
CD24+
Ectoderm-like cells
mESC
72h
Differentiation media
72h
CD140a+
Extraembryonic endoderm
(XEN)
b
LIF
RA
CD24 intensity (a.u.)
CD140a intensity (a.u.)
RiboBright intensity (a.u.)
c
Q1
Q2
Q3
Q4
CD24 Intensity
CD140a Intensity
Q1: CD24+ CD140a-
Q2: CD24+ CD140a+
Q3: CD24- CD140a+
Q4: CD24- CD140a-
Density
Mean
Normalized RiboBright Intensity
d
CD140a
RiboBright
CD24
Overlay
40 μm
10 μm
e
Average RiboBright Intensity per cell (a.u.)
ns
CD24- CD140a-
CD24+
CD140a+
f
Cell Area (μm²*100)
g
Super
Normal
Confined
Average Diffusion Coefficient (μm²s⁻¹)

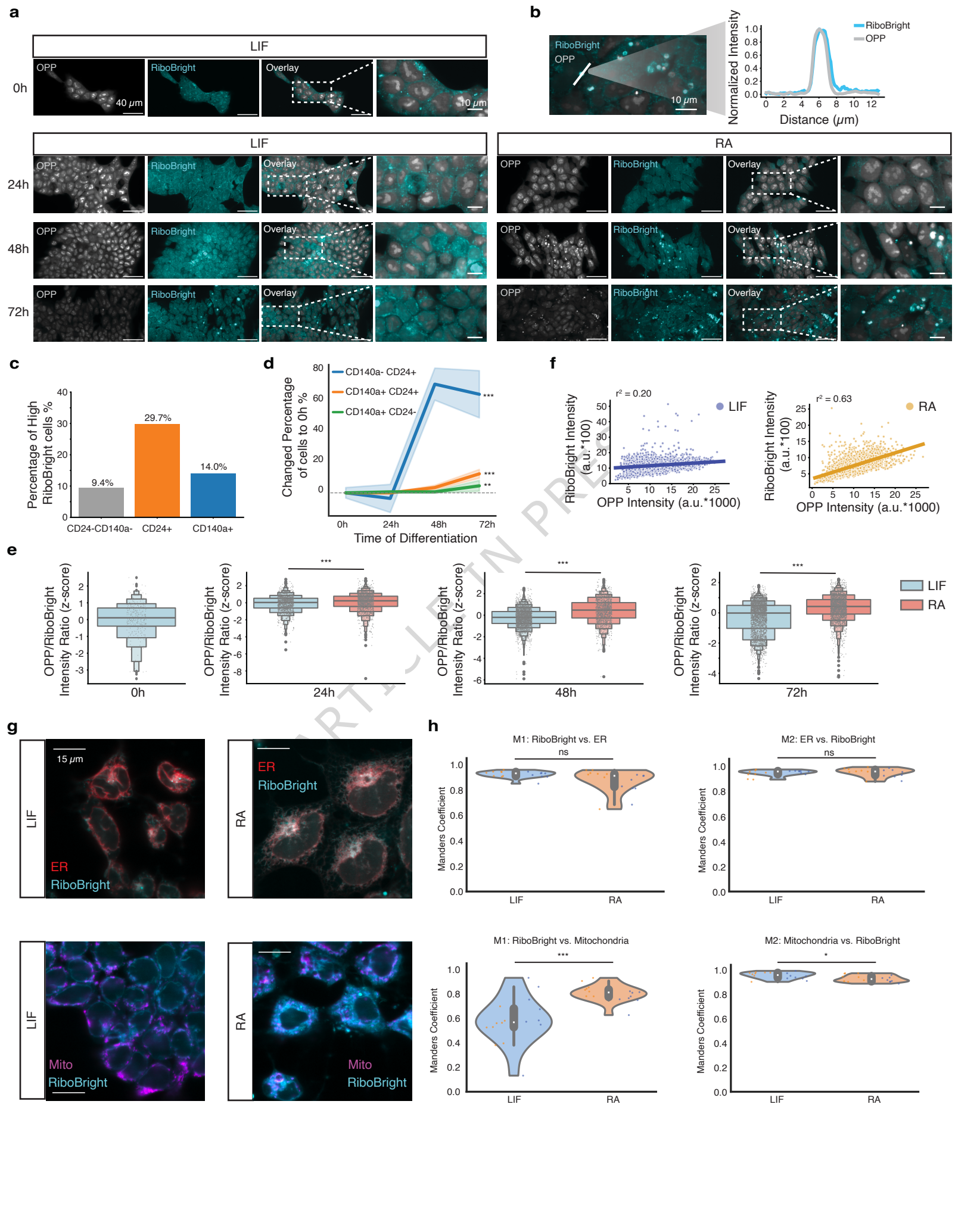
a
LIF
0h
OPP
RiboBright
Overlay
40 μm
10 μm
b
RiboBright
OPP
10 μm
Normalized Intensity
RiboBright
OPP
Distance (μm)
LIF
RA
24h
48h
72h
c
Percentage of High RiboBright cells %
9.4%
29.7%
14.0%
CD24-CD140a-
CD24+
CD140a+
d
CD140a- CD24+
CD140a+ CD24+
CD140a+ CD24-
Changed Percentage of cells to 0h %
Time of Differentiation
f
r² = 0.20
r² = 0.63
LIF
RA
RiboBright Intensity (a.u.*100)
OPP Intensity (a.u.*1000)
e
OPP/RiboBright Intensity Ratio (z-score)
0h
24h
48h
72h
g
15 μm
ER
RiboBright
Mito
h
M1: RiboBright vs. ER
M2: ER vs. RiboBright
M1: RiboBright vs. Mitochondria
M2: Mitochondria vs. RiboBright
Manders Coefficient
ns